Optical Coherence Tomography: Advanced Modeling

17

Peter E. Andersen, Lars Thrane, Harold T. Yura, Andreas Tycho, and Thomas M. Jørgensen

Contents

P.E. Andersen (✉) • L. Thrane • A. Tycho • T.M. Jørgensen
Department of Photonics Engineering, Technical University of Denmark, Kongens Lyngby, Denmark
e-mail: peta@fotonik.dtu.dk, lath@fotonik.dtu.dk, tmjq@fotonik.dtu.dk

H.T. Yura
Electronics and Photonics Laboratory, The Aerospace Corporation, Los Angeles, CA, USA
e-mail: hal.t.yura@aero.org

V.V. Tuchin (ed.), *Handbook of Coherent-Domain Optical Methods*,
DOI 10.1007/978-1-4614-5176-1_17,

Abstract

Analytical and numerical models for describing and understanding the light propagation in samples imaged by optical coherence tomography (OCT) systems are presented. An analytical model for calculating the OCT signal based on the extended Huygens-Fresnel principle valid both for the single- and multiple-scattering regimes is derived. An advanced Monte Carlo model for calculating the OCT signal is also derived, and the validity of this model is shown through a mathematical proof based on the extended Huygens-Fresnel principle. From the analytical model, an algorithm for enhancing OCT images is developed, the so-called true-reflection algorithm in which the OCT signal may be corrected for the attenuation caused by scattering. The algorithm is verified experimentally and by using the Monte Carlo model as a numerical tissue phantom. Applications of extraction of optical properties from tissue are discussed. Finally, the Wigner phase-space distribution function is derived in a closed-form solution, which may have applications in OCT.

17.1 Introduction

Optical coherence tomography (OCT) has developed rapidly since its potential for applications in clinical medicine was first demonstrated in 1991 [1]. OCT performs high-resolution, cross-sectional tomographic imaging of the internal microstructure in materials and biologic systems by measuring backscattered or backreflected light.

Mathematical models [2–9] have been developed to promote understanding of the OCT imaging process and thereby enable development of better imaging instrumentation and data processing algorithms. One of the most important issues in the modeling of OCT systems is the role of the multiple-scattered photons, an issue, which only recently has become fully understood, the works of Thrane et al. [10] and Turchin et al. [11] representing the most comprehensive modeling. Hence, such modeling, capable of describing both the single- and multiple-scattering regimes simultaneously in heterogeneous media, is essential in order to completely describe the behavior of OCT systems.

Experimental validation of models on realistic sample structures, for example, layered sample structures, would require manufacturing of complex tissue phantoms with well-controlled optical properties. However, a useful alternative to validate the analytical predictions on such geometries is to apply a Monte Carlo

(MC)-based simulation model [12], since there are few limitations on which geometries that may be modeled using MC simulations. MC models for analyzing light propagation are based on simulating the radiative equation of transfer by tracing a large number of energy packets, each considered to represent a given fraction of the incident light energy [13, 14]. Hence, as a numerical experiment, one has full control of all parameters.

The scope of this chapter is the presentation of analytical and numerical models that are able to describe the performance of OCT systems including multiple-scattering effects in heterogeneous media. Such models, where the contribution to the OCT signal from multiple-scattering effects has been taken into account, are essential for the understanding and in turn optimization of OCT systems. Moreover, establishing a valid MC model of OCT systems is important, because such a model may serve as a numerical phantom providing data that are otherwise cumbersome to obtain experimentally. In general, these models, analytical as well as numerical, may serve as important tools for improving interpretation of OCT images.

17.1.1 Organization of This Chapter

The chapter is divided into four sections, covering specific topics in modeling OCT systems. In Sect. 17.2, an analytical model for the detected OCT signal is derived based on the extended Huygens-Fresnel principle. In the field of biomedical optics, Monte Carlo simulations have already proved their value. In Sect. 17.3, an advanced Monte Carlo model for calculating the OCT signal is presented, and comparisons to the analytical model are made. The analytical model, in Sect. 17.4, is then used to derive the optical properties of a scattering medium, which forms the basis of the so-called true-reflection algorithm. The algorithm is verified using MC simulations as well as experiments. The Wigner phase-space distribution function has been proposed as an alternative to OCT. In Sect. 17.5, we demonstrate the applicability of using the extended Huygens-Fresnel principle to calculate the Wigner phase-space distribution function and to derive a novel method of OCT imagery.

17.2 Analytical OCT Model Based on the Extended Huygens-Fresnel Principle

Since the first paper describing the use of the OCT technique for noninvasive cross-sectional imaging in biological systems [1], various theoretical models of the OCT system have been developed. The primary motivation has been optimization of the OCT technique, thereby improving the imaging capabilities. The first theoretical models were based on single-scattering theory [2, 3]. These models are restricted to superficial layers of highly scattering tissue in which only single scattering occurs. Single scattering or single backscattering refers to photons which do not undergo scattering either to or from the backscattering plane of interest, that is, ballistic photons.

At larger probing depths, however, the light is also subject to multiple scattering. The effects of multiple scattering have been investigated on an experimental basis [4] and by using a hybrid Monte Carlo/analytical model [5], analysis methods of linear systems theory [6], on the basis of solving the radiative transfer equation in the small-angle approximation [7], a model based on the extended Huygens-Fresnel (EHF) principle [8], and MC simulations [9]. Note that modeling using MC simulations is treated in greater detail in Sect. 17.3.3.

In the present context, the main objective is the analysis of multiple-scattering effects. As shown by several investigations, the primary effects of multiple scattering are a reduction of the imaging contrast and resolution of the OCT system.

In Ref. [15], the authors suggested solving the multiple-scattering problem by using the EHF principle [8] known from atmospheric propagation of laser beams [16]. Their analysis contains one important inaccuracy because in their end result, the ballistic component is included twice, leading to erroneous calculations. As a result, their analysis should be applied with care. In addition, the effects of the so-called shower-curtain effect [16] are not accounted for in their analysis. Thrane et al. [10] succeeded in applying the EHF principle for the OCT geometry (see below). Following their analysis, Feng et al. [17] aimed at expanding on the use of EHF in modeling the OCT geometry. In particular, their aim is to simplify the analysis, but several mistakes are introduced in the attempt: Firstly, an imaginary lens is introduced with the purpose of obviating the shower-curtain effect, leading to errors in the final calculation of the OCT signal. Secondly, an erroneous lateral coherence length is introduced, that is, the lateral coherence length should be calculated as resulting from reflecting off a rough surface and not, as done in Ref. [17], a specular surface. Hence, their model should be approached with caution.

A statistical optics approach to adequately model the effects of multiple scattering was proposed by Karamata et al. [18]. However, their analysis, based on a heuristic argument, is misleading and incorrect. The main error is due to their assumption regarding spatial coherence, where it is alleged that transverse spatial coherence is not degraded due to multiple scattering. The argument used by Karamata et al. [18] is valid only for the case of a focused beam reflecting off a rough surface with no scattering medium in between the reflection site and the collection aperture (see, e.g., pages 210–211 of Ref. [19]). This is definitely not the case for OCT in turbid media (i.e., tissue). The degradation of spatial coherence of a beam propagating through a multiple-scattering media is well known and documented in the literature (see Ref. [20] and references therein). Therefore, the analysis given in Ref. [18] is not considered further, and the results and conclusions should not be used in modeling light propagation in turbid media.

Recently, Turchin et al. [11] expanded the analysis of Dolin [7] to an OCT geometry. Their analysis is based on the radiative transfer equation (RTE) in the small-angle approximation, of which Arnush [21] first obtained the closed-form solution. It should be noted that in this approximation, the solution of the RTE and the EHF is identical [22, 23]. In general, the analysis of Ref. [11] is consistent with that of the EHF model, which is presented below. However, technically there are two important differences that need to be pointed out. Firstly, the choice of

scattering phase function in Ref. [11]: as in Ref. [10], the forward scattered part is modeled by a Gaussian distribution, but additionally a small backscattered fraction is included. This way of taking into account tissue backscattering was previously suggested by Raymer and coworkers [24] and discussed by Yura et al. [23]. However, it was not included in the EHF analysis of the OCT geometry [10], but it can be readily adopted [25]. Hence, the RTE [11] and EHF [10] descriptions are equivalent. Secondly, Thrane et al. [10] present an analytic engineering expression for the OCT signal current based on an accurate analytical approximation for the irradiance distribution in the backscatter plane (see Sect. 17.7 for details). Turchin et al. [11] do not use this approximation, and consequently their end results require numerical computations, which yield highly accurate values for the OCT signal current. They also obtain accurate results in the extraction of optical scattering properties of the sample, which is further addressed in at the end of this chapter. Furthermore, it is noted that the analysis of Turchin et al. [11] is restricted to the special case where the focusing lens in the sample arm is in direct contact with the tissue being investigated. This is in contrast to the analysis of Ref. [10] where the ABCD ray-matrix formalism was used to readily include an arbitrary configuration of the sample arm. Finally, in contrast to the totally numerical results of Ref. [11], the multiple-scattering EHF analysis presented below yields accurate analytic expressions for the OCT signal for a wide range of optical configurations that are both amenable to physical interpretation and are desirable for use in parametric studies for OCT system optimization.

In this section, a general theoretical description [10, 26–28] of the OCT technique when used for imaging in highly scattering tissue is presented. The description is based on the EHF principle. It is shown that the theoretical model, based on this principle and the use of mutual coherence functions, simultaneously describes the performance of the OCT system in both the single- and multiple-scattering regimes. In a standard OCT system [1] with diffuse backscattering from the tissue discontinuity being probed, and a distance between the focusing lens and the tissue, the so-called shower-curtain effect [16, 29, 30] is present. This effect has been omitted in previous theoretical models [8]. However, it is demonstrated in this section that inclusion of this effect is of utmost importance in the theoretical description of an OCT system.

17.2.1 The Extended Huygens-Fresnel Principle

When an optical wave propagates through a random medium, for example, tissue, both the amplitude and phase of the electric field experience random fluctuations caused by small random changes in the index of refraction. Several different theoretical approaches have been developed for describing these random amplitude and phase fluctuations, based upon solving the wave equation for the electric field of the wave or for the various statistical moments of the field. By assuming a sinusoidal time variation in the electric field, it has been shown [31–34] that

Maxwell's equations for the vector amplitude $\mathbf{E}(\mathbf{R})$ of a propagating electromagnetic wave through a non-absorbing refracting medium lead directly to

$$\nabla^2\mathbf{E} + k^2 n^2(\mathbf{R})\mathbf{E} + 2\nabla[\mathbf{E}\cdot\nabla \ln n(\mathbf{R})] = 0, \tag{17.1}$$

where $\mathbf{R}$ denotes a point in space, k is the wave number of the electromagnetic wave, and $n(\mathbf{R})$ is the index of refraction whose time variations have been suppressed. We now assume that the magnitude of the index of refraction fluctuations is small in comparison with unity. Hence, the index of refraction $n(\mathbf{R}) = \langle n(\mathbf{R})\rangle + n_f(\mathbf{R})$, where $n_f(\mathbf{R})$ is the small fluctuating part of the index of refraction with zero mean and a root-mean-square value much less than unity. This assumption is in general valid for tissue [35]. In this case, it has been shown that the last term on the left-hand side of (17.1), which is related to the change in polarization of the wave as it propagates, is negligible if the wavelength of the radiation $\lambda \ll 2\pi\, l_0$, where l_0 is a measure of the smallest random inhomogeneities in the medium [33, 34]. The structures that dominate light propagation in tissue, for example, cells, have a size of 2 μm or more, which means that the criteria for neglecting the depolarization term are fulfilled in the case of interest where $\lambda \sim 1.0$ μm. By dropping this term, (17.1) simplifies to

$$\nabla^2\mathbf{E} + k^2 n(\mathbf{R})\mathbf{E} = 0, \tag{17.2}$$

which is now easily decomposed into three scalar equations, one for each component of the field $\mathbf{E}$. If we let $U(\mathbf{R})$ denote one of the scalar components transverse to the direction of propagation along the positive z-axis, then (17.2) may be replaced by the scalar stochastic equation

$$\nabla^2 U + k^2 n^2(\mathbf{R})U = 0. \tag{17.3}$$

Equation (17.3) cannot be solved exactly in closed form. Some early attempts to solve (17.3) were based on the geometric optics approximation [36], which ignores diffraction effects, and on perturbation theories widely known as the Born approximation and Rytov approximation [32]. One approach to solving (17.3) by other than perturbation methods was developed, independent of each other, by Lutomirski and Yura [37] and by Feizulin and Kravtsov [38]. This technique is called the extended Huygens-Fresnel (EHF) principle. As the name indicates, it is an extension of the Huygens-Fresnel principle to a medium that exhibits a random spatial variation in the index of refraction. That is, the field due to some arbitrary complex disturbance specified over an aperture can be computed, for propagation distances that are large compared with the size of the aperture, by superimposing spherical wavelets that radiate from all elements of the aperture. This principle follows directly from Green's theorem [39] and the Kirchhoff approximation [39] applied to the scalar wave equation together with a field reciprocity theorem between an observation point and a source point of spherical waves in the random medium. On the basis of this principle, the geometry of the problem, that is, the

aperture field distribution, can be separated from the propagation problem, which is determined by the way a spherical wave propagates through the medium. Furthermore, Yura and Hanson [40, 41] have applied the EHF principle to paraxial wave propagation through an arbitrary ABCD system in the presence of random inhomogeneities. An arbitrary ABCD system refers to an optical system that can be described by an ABCD ray-transfer matrix [42]. In the cases of interest in this section, the ABCD ray-transfer matrix is real, and the field in the output plane is then given by [40]

$$U(\mathbf{r}) = \int U_0(\mathbf{p}) G(\mathbf{p}, \mathbf{r}) d\mathbf{p}, \tag{17.4}$$

where $\mathbf{r}$ and $\mathbf{p}$ are two-dimensional vectors transverse to the optical axis in the output plane and input plane, respectively. Throughout this chapter it is understood that spatial integrals are to be carried out over the entire plane in question.

The quantity $U_0(\mathbf{p})$ is the field in the input plane, and $G(\mathbf{p},\mathbf{r})$ is the EHF Green's function response at $\mathbf{r}$ due to a point source at $\mathbf{p}$ given by [37, 40]

$$G(\mathbf{p}, \mathbf{r}) = G_0(\mathbf{p}, \mathbf{r}) \exp[i\varphi(\mathbf{p}, \mathbf{r})], \tag{17.5}$$

where $G_0(\mathbf{p},\mathbf{r})$ is the Huygens-Fresnel Green's function for propagation through an ABCD system in the absence of random inhomogeneities and $\varphi(\mathbf{p},\mathbf{r})$ is the random phase of a spherical wave propagating in the random medium from the input plane to the output plane. The Huygens-Fresnel Green's function $G_0(\mathbf{p},\mathbf{r})$ is given by [40]

$$G_0(\mathbf{p}, \mathbf{r}) = -\frac{ik}{2\pi B} \exp\left[-\frac{ik}{2B}\left(Ap^2 - 2\mathbf{p}\cdot\mathbf{r} + Dr^2\right)\right], \tag{17.6}$$

where A, B, and D are the ray-matrix elements for propagation from the input plane to the output plane. In the following, it is assumed that φ is a normally distributed zero-mean random process.

17.2.2 The OCT Signal

A conventional OCT system [1] consists of a superluminescent diode (SLD), a Michelson interferometer with movable reference mirror, and a photodetector. The rotationally symmetric sample arm geometry of the OCT system is shown in Fig. 17.1. The tissue discontinuity being probed arises from a refractive index discontinuity between two tissue layers ($n \neq n_1$ in Fig. 17.1). Therefore, the discontinuity, located at a depth z in the tissue, is characterized by a Fresnel reflection coefficient R_d. A lens with focal length f is placed at a distance d from the tissue surface. In the system of interest, the focal plane coincides with the tissue discontinuity. Furthermore, the reference arm optical path length in the Michelson interferometer is matched to the focal plane optical depth.

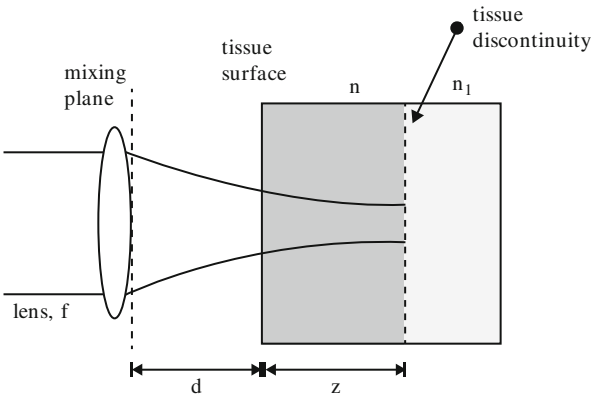

Fig. 17.1 Sample arm geometry of the OCT system (From Ref. [10])

In the case of human skin, light scattering in the bulk tissue is predominantly in the forward direction for the wavelengths of interest in the NIR region [43]. Hence, we neglect bulk backscattering and use the EHF principle [37, 38] to describe the light propagation in the bulk tissue. This is justified by the fact that the EHF principle is based on the paraxial approximation and therefore valid for small-angle forward scattering. In particular, it can be shown that the paraxial approximation is valid up to 30°, that is, 0.5 rad [42]. Because most tissues are characterized by *rms* scattering angles below this limit, the EHF principle may be used to describe light propagation in tissue, retaining both amplitude and phase information. Also, the bulk tissue absorption is neglected [43]. Thus, the bulk tissue is characterized by a scattering coefficient μ_s, a root-mean-square scattering angle θ_{rms} or asymmetry parameter g [44], and a mean index of refraction n. Furthermore, the bulk tissue is modeled as a material with scatterers randomly distributed over the volume of interest. Note that in the present analysis, polarization effects are excluded.

By mixing the sample field U_S reflected from the discontinuity in the tissue at depth z, with the reference field U_R on the photodetector of the OCT system, we obtain that the heterodyne signal current $i(z)$ can be expressed as [8]

$$i(z) \propto \mathrm{Re}\left[\int U_R(\mathbf{p},t)U_S^*(\mathbf{p},t+\tau)d\mathbf{p}\right], \tag{17.7}$$

where the integration is taken over the area of the photodetector, Re denotes the real part, and τ is the difference between the propagation times of the reference and sample beams. In practice, the heterodyne signal current $i(z)$ is measured over a time much longer than the source coherence time. In this case, it can be shown that [8]

$$i(z) \propto |g(\tau)|\mathrm{Re}\left[\int U_R(\mathbf{p})U_S^*(\mathbf{p})d\mathbf{p}\right], \tag{17.8}$$

where $|g(\tau)|$ is the modulus of the normalized temporal coherence function of the source (notice that $g(\tau)$ is not related to the asymmetry parameter g).

Because the detailed structure of the tissue is unknown a priori, it is necessary and appropriate to treat the optical distortions as a random process and, as is commonly done in the literature, to specify certain measures of the average performance, for example, the mean (i.e., ensemble average) square heterodyne signal current. It can be shown that the mean square heterodyne signal current $\langle i^2(z)\rangle$, which is proportional to the heterodyne signal power, is given by [8, 29]

$$\langle i^2(z)\rangle = 2\alpha^2|g(\tau)|^2 \mathrm{Re}\left[\int\int \Gamma_S(\mathbf{p}_1,\mathbf{p}_2;z)\Gamma_R(\mathbf{p}_1,\mathbf{p}_2)d\mathbf{p}_1 d\mathbf{p}_2\right], \tag{17.9}$$

where

$$\Gamma_R(\mathbf{p}_1,\mathbf{p}_2) = U_R(\mathbf{p}_1)U_R^*(\mathbf{p}_2), \tag{17.10}$$

$$\Gamma_S(\mathbf{p}_1,\mathbf{p}_2;z) = \langle U_S(\mathbf{p}_1;z)U_S^*(\mathbf{p}_2;z)\rangle \tag{17.11}$$

are the mutual coherence functions of the reference and the reflected sample optical fields in the mixing plane. The angular brackets denote an ensemble average both over the statistical properties of the tissue and the reflecting discontinuity. For simplicity, the heterodyne mixing process has been chosen to take place directly behind the lens at the side facing the tissue, and $\mathbf{p}_1$, $\mathbf{p}_2$ are two-dimensional vectors in this plane transverse to the optical axis. The quantity α is a conversion factor for power to current and equals $(q_e\eta/h\nu)$, where q_e is the electronic charge, η the detector quantum efficiency, ν the optical frequency, and h the Planck's constant. In the case of interest, the reference arm optical path length in the Michelson interferometer is always matched to the sample arm optical path length, from which it follows that $|g(\tau)| = |g(0)| = 1$ [8].

For the heterodyne detection scheme, the spatial coherence properties of the sample field contained in the mutual coherence function Γ_S are of utmost importance in the determination of the corresponding signal. In particular, if the spatial coherence of the sample field is degraded with respect to the reference field, one obtains a corresponding degradation in the signal-to-noise ratio.

The reference field and the input sample field U_{Si} in the lens plane impinging on the sample are assumed to be of Gaussian shape and given by

$$U_R(\mathbf{p},t) = \sqrt{\frac{P_R}{\pi w_0^2}}\exp\left[-\frac{p^2}{2}\left(\frac{1}{w_0^2}+\frac{ik}{f}\right)\right]\exp[i\omega_R t + \varphi_R(t)], \tag{17.12}$$

$$U_{Si}(\mathbf{p},t) = \sqrt{\frac{P_R}{\pi w_0^2}}\exp\left[-\frac{p^2}{2}\left(\frac{1}{w_0^2}+\frac{ik}{f}\right)\right]\exp[i\omega_S t], \tag{17.13}$$

where P_R and P_S are the powers of the reference and input sample beams, respectively, w_0 is the $1/e$ intensity radius of these beams in the lens plane, $k = 2\pi/\lambda$, where λ is the center wavelength of the source in vacuum, ω_R and ω_S are the angular frequencies of the reference and input sample beams, respectively, and φ_R is the phase of the reference field relative to the input sample field.

In the determination of the mutual coherence function Γ_S, we use the EHF principle to obtain a viable expression for $U_S(\mathbf{p};z)$, that is, the reflected sample optical field in the mixing plane. Using (17.4), we have

$$U_S(\mathbf{p};z) = \int U_B(\mathbf{r};z)G(\mathbf{r},\mathbf{p};z)d\mathbf{r}, \tag{17.14}$$

where $U_B(\mathbf{r};z)$ is the reflected sample field in the plane of the tissue discontinuity, $\mathbf{r}$ is a two-dimensional vector in this plane transverse to the optical axis, and $G(\mathbf{r},\mathbf{p};z)$ is the EHF Green's function response at $\mathbf{p}$ due to a point source at $\mathbf{r}$, which includes the effects of scattering in the intervening medium. Combining (17.11) and (17.14) yields

$$\Gamma_S(\mathbf{p}_1,\mathbf{p}_2;z) = \iint \langle U_B(\mathbf{r}_1;z)U_B(\mathbf{r}_2;z)G(\mathbf{r}_1,\mathbf{p}_1;z)G^*(\mathbf{r}_2,\mathbf{p}_2;z)\rangle d\mathbf{r}_1 d\mathbf{r}_2, \tag{17.15}$$

where $\mathbf{r}_1$, $\mathbf{r}_2$ are two-dimensional vectors in this plane transverse to the optical axis. For simplicity in notation, we omit in the following the explicit dependence of the various quantities on z.

We next assume that the statistical properties of the bulk tissue and the tissue discontinuity are independent and that the propagation to the tissue discontinuity is statistically independent from the corresponding reflected propagation path. The former seems to be a reasonable assumption for a medium like tissue. The latter means that enhanced backscattering is neglected. Enhanced backscattering and the criterion for neglecting it are discussed in Sect. 17.5. From these assumptions, it follows that

$$\begin{aligned}&\langle U_B(\mathbf{r}_1)U_B^*(\mathbf{r}_2)G(\mathbf{r}_1,\mathbf{p}_1)G^*(\mathbf{r}_2,\mathbf{p}_2)\rangle = \\ &\langle U_B(\mathbf{r}_1)U_B^*(\mathbf{r}_2)\rangle\langle G(\mathbf{r}_1,\mathbf{p}_1)G^*(\mathbf{r}_2,\mathbf{p}_2)\rangle.\end{aligned} \tag{17.16}$$

The first term on the right-hand side of (17.16) relates to both the mean value over statistics of the bulk tissue in propagating from the lens plane to the tissue discontinuity and the reflection statistics of the discontinuity. The second term on the right-hand side of (17.16) relates to the corresponding average over the statistics of the bulk tissue when propagating back from the discontinuity to the mixing plane. Assuming diffuse backscattering from the tissue discontinuity, we have [29, 45]

$$\langle U_B(\mathbf{r}_1)U_B^*(\mathbf{r}_2)\rangle = \frac{4\pi}{k^2}\delta(\mathbf{r}_1-\mathbf{r}_2)\langle I_B(\mathbf{r}_1)\rangle, \tag{17.17}$$

where $\delta(\mathbf{r})$ is the two-dimensional Dirac delta function and $I_B(\mathbf{r}_1)$ is the mean backscattered irradiance distribution in the plane of the discontinuity. An adequate analytic approximation for this mean backscattered irradiance distribution is obtained by multiplying the approximate expression for the mean irradiance distribution, derived in Sect. 17.2.3, by the reflection coefficient R_d. The expression, which is valid for arbitrary values of the optical depth $\mu_s z$, is given by

$$\langle I_B(r)\rangle = \frac{R_d P_S}{\pi}\left[\frac{e^{-\mu_S z}\exp\left[-r^2/w_H^2\right]}{w_H^2} + \frac{(1-e^{-\mu_S z})\exp\left[-r^2/w_S^2\right]}{w_S^2}\right]. \tag{17.18}$$

The first term in the brackets on the right-hand side of (17.18) can be interpreted to represent the attenuated distribution obtained in the absence of the inhomogeneities, and the corresponding second term represents a broader halo resulting from scattering by the inhomogeneities. The quantities w_H and w_S are the $1/e$ irradiance radii or spot sizes in the discontinuity plane in the absence and presence of scattering, respectively, given by

$$w_H^2 = w_0^2\left(A - \frac{B}{f}\right)^2 + \left(\frac{B}{kw_0}\right)^2, \tag{17.19}$$

$$w_S^2 = w_0^2\left(A - \frac{B}{f}\right)^2 + \left(\frac{B}{kw_0}\right)^2 + \left(\frac{2B}{k\rho_0}\right)^2. \tag{17.20}$$

A and B are the ray-matrix elements for propagation from the lens plane to the discontinuity plane. For the geometry of interest, A and B are given by $A = 1$ and $B = f = d + z/n$ [42]. The quantity ρ_0 appearing in (17.20) is the lateral coherence length of a spherical wave in the lens plane due to a point source in the discontinuity plane [29]. The lateral coherence length is discussed in detail in Ref. [10].

Combining (17.15), (17.16), and (17.17) and simplifying yield

$$\Gamma_S(\mathbf{p}_1, \mathbf{p}_2) = \frac{4\pi}{k^2}\int \langle I_B(\mathbf{r})\rangle\langle G(\mathbf{r}, \mathbf{p}_1)G^*(\mathbf{r}, \mathbf{p}_2)\rangle d\mathbf{r}. \tag{17.21}$$

Using (17.5), the second term in the integral on the right-hand side of (17.21) may be written as

$$\langle G(\mathbf{r}, \mathbf{p}_1)G^*(\mathbf{r}, \mathbf{p}_2)\rangle = G_0(\mathbf{r}, \mathbf{p}_1)G_0^*(\mathbf{r}, \mathbf{p}_2)\Gamma_{pt}(\rho), \tag{17.22}$$

where $G_0(\mathbf{r},\mathbf{p})$ is the Huygens-Fresnel Green's function when propagating from the discontinuity plane to the lens plane and Γ_{pt} is the mutual coherence function of a point source located in the discontinuity plane and observed in the lens plane given by

$$\Gamma_{pt} = \langle\exp[i\{\phi(\mathbf{p}_1) - \phi(\mathbf{p}_2)\}]\rangle. \tag{17.23}$$

The mutual coherence function Γ_{pt} contains the effects of the scattering inhomogeneities. Using (17.6), the Green's function $G_0(\mathbf{r},\mathbf{p})$ is given by

$$G_0(\mathbf{r},\mathbf{p}) = -\frac{ik}{2\pi B_b}\exp\left[-\frac{ik}{2B_b}\left(A_b r^2 - 2\mathbf{r}\cdot\mathbf{p} + D_b p^2\right)\right], \tag{17.24}$$

where A_b, B_b, and D_b are the ray-matrix elements for backpropagation to the lens plane. These quantities are given by $A_b = D = 1$, $B_b = B = d + z/n$, and $D_b = A = 1$ [40]. In order to obtain an analytical solution, we have to use an approximate expression for the mutual coherence function Γ_{pt}. The expression, derived in Sect. 17.2.3, is given by

$$\Gamma_{pt}(\rho) \cong e^{-\mu_s z} + (1 - e^{-\mu_s z})\exp\left[-\rho^2/\rho_0^2\right], \tag{17.25}$$

where $\rho = |\mathbf{p}_1 - \mathbf{p}_2|$.

Substituting (17.10), (17.12), (17.18), (17.21), (17.22), (17.24), and (17.25) into (17.9) and performing the indicated Gaussian integrations over $\mathbf{p}_1$,$\mathbf{p}_2$ and simplifying yield

$$\begin{aligned}\left\langle i^2(z)\right\rangle = &\frac{2\alpha^2 P_R P_S \sigma_b}{\pi^2} \\ &\times \int\left[\frac{e^{-\mu_S z}\exp\left[-r^2/w_H^2\right]}{w_H^2} + \frac{(1 - e^{-\mu_S z})\exp\left[-r^2/w_S^2\right]}{w_S^2}\right] d\mathbf{r},\end{aligned} \tag{17.26}$$

where the effective backscattering cross section of the tissue discontinuity $\sigma_b = 4\pi R_d/k^2$. It is important to note that the algebraically simple result given in (17.26) is, strictly speaking, valid only for propagation geometries where $A = D$, as is obtained in the case of interest. Performing the integration over the discontinuity plane in (17.26) and simplifying, we obtain the following expression for the mean square heterodyne signal current

$$\begin{aligned}\left\langle i^2(z)\right\rangle = &\frac{\alpha^2 P_R P_S \sigma_b}{\pi w_H^2} \\ &\times \left[e^{-2\mu_s z} + \frac{2e^{-\mu_s z}(1 - e^{-\mu_s z})}{1 + \frac{w_S^2}{w_H^2}} + (1 - e^{-\mu_s z})^2\frac{w_H^2}{w_S^2}\right] \\ \equiv &\left\langle i^2\right\rangle_0 \Psi(z).\end{aligned} \tag{17.27}$$

The quantity $\left\langle i^2\right\rangle_0 = \alpha^2 P_R P_S \sigma_b/\pi(w_H)^2$ is the mean square heterodyne signal current in the absence of scattering, and the terms contained in the brackets are the heterodyne efficiency factor $\Psi(z)$. A comparison between the analytic approximation of $\Psi(z)$, given in (17.27), and the exact numerical calculation is given in Ref. [46]. Physically, $\Psi(z)$ can be looked upon as the reduction in the heterodyne signal-to-noise ratio due to the scattering of the tissue. The first term in the brackets

of (17.27) represents the contribution due to single scattering. The corresponding third term is the multiple-scattering term, and the second term is the cross term. Physically, the cross term is the coherent mixing of the unscattered and the multiple-scattered light.

17.2.2.1 Dynamic Focusing: Diffuse Reflectance

When the focal plane coincides with the tissue discontinuity, that is, $fA = B$ with $A = 1$, we obtain from (17.19) and (17.20)

$$w_H^2 = \left(\frac{f}{kw_0}\right)^2; \quad \frac{w_H^2}{w_S^2} = \frac{1}{1 + \left(\frac{2w_0}{\rho_0(z)}\right)^2}. \tag{17.28}$$

The quantity $\rho_0(z)$ is the lateral coherence length of the reflected sample field in the mixing plane. For lateral separations much less (greater) than $\rho_0(z)$, the field can be considered to be mutually coherent (incoherent). Because of the diffuse back-scattering from the tissue discontinuity, $\rho_0(z)$ is determined only by the propagation back through the tissue from the tissue discontinuity to the mixing plane. As a consequence, $\rho_0(z)$ is the lateral coherence length of a point source located in the tissue discontinuity plane, as observed in the mixing plane. For the geometry of interest, it can be shown [46] that

$$\rho_0(z) = \sqrt{\frac{3}{\mu_s z}} \frac{\lambda}{\pi \theta_{rms}} \left(1 + \frac{nd(z)}{z}\right), \tag{17.29}$$

where $d(z) = f - (z/n)$ and $\theta_{rms} \approx [2(1 - g)]^{1/2}$. The second term in the brackets of (17.29) indicates that the lateral coherence length increases with increasing distance between the tissue surface and the mixing plane.

This well-known dependence of the lateral coherence length on the position of the scattering medium relative to the observation plane is the so-called shower-curtain effect [29, 30]. In general, the shower-curtain effect implies that the lateral coherence length obtained for the case when the scattering medium is close to the radiation source is larger than for the case when the scattering medium is close to the observation plane. Physically, this is due to the fact that a distorted spherical wave approaches a plane wave as it further propagates through a non-scattering medium. As a consequence, for example, from a distance, one can see a person immediately behind a shower curtain, but the person cannot see you. The effect is well known for light propagation through the atmosphere as discussed by Dror et al. [30] but has been omitted in previous theoretical OCT models [8]. However, due to the finite distance between the focusing lens and the tissue, the effect is inevitably present in practical OCT systems and could facilitate system optimization [46]. Finally, the reflection characteristics of the tissue discontinuity play a vital role for the shower-curtain effect.

17.2.2.2 Dynamic Focusing: Specular Reflectance

If we, instead of diffuse backscattering, had a specular reflection at the tissue discontinuity, the corresponding mutual coherence function for plane waves would apply. Using this mutual coherence function, we have

$$\Psi(z) = \left[e^{-2\mu_s z} + \left(1 - e^{-2\mu_s z}\right) \frac{w_H^2}{w_S^2} \right] \tag{17.30}$$

and

$$\rho_0(z) = \sqrt{\frac{1}{2\mu_s z}} \frac{\lambda}{\pi \theta_{rms}}. \tag{17.31}$$

It is obvious from (17.31) that the shower-curtain effect would not be present in the case of specular reflection at the tissue discontinuity, in contrast to the case of diffuse backscattering. However, it is important to note that it is diffuse backscattering which actually occurs in the case of (skin) tissue.

17.2.2.3 Collimated Sample Beam

In the case of a collimated sample beam, the expressions for w_H and w_S in (17.19) and (17.20) need to be rewritten:

$$w_H^2 = \lim_{f \to \infty} \left[w_0^2 \left(1 - \frac{d + \frac{z}{n}}{f} \right)^2 + \left(\frac{d + \frac{z}{n}}{k w_0} \right)^2 \right] = w_0^2 + \left(\frac{d + \frac{z}{n}}{k w_0} \right)^2 \tag{17.32}$$

$$w_S^2 = \lim_{f \to \infty} \left[w_H^2 + \left(\frac{2\left(d + \frac{z}{n}\right)}{k \rho_0} \right)^2 \right] = w_0^2 + \left(\frac{d + \frac{z}{n}}{k w_0} \right)^2 + \left(\frac{2\left(d + \frac{z}{n}\right)}{k \rho_0} \right)^2, \tag{17.33}$$

where it has been used that $A = 1$ and $B = d + z/n$ and note that now $B \neq f$. In order to find the heterodyne efficiency factor, these expressions must be inserted in (17.27), and moreover, the expression for ρ_0 should be chosen in accordance with the reflection characteristics of the probed discontinuity.

17.2.2.4 Numerical Results

The heterodyne efficiency factor $\Psi(z)$ is shown as a function of depth z of the tissue discontinuity in Fig. 17.2 for typical parameters of human skin tissue with diffuse backscattering and the shower-curtain effect included (dashed) and specular reflection (solid), respectively. For comparison, we show the case of diffuse backscattering with exclusion of the shower-curtain effect (dash-dot) and the case of pure single scattering (dotted). At shallow depths, single backscattering dominates. Due to multiple scattering, the slope is changed and $\Psi(z)$ becomes almost constant for three cases (curves 1–3). The important difference is, however, that the change of

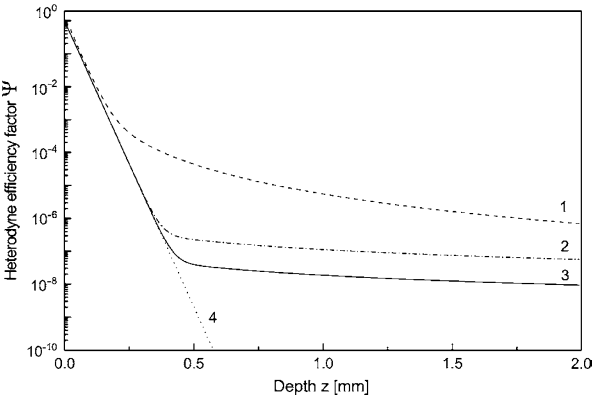

Fig. 17.2 $\Psi(z)$ as a function of z for diffuse backscattering with the shower-curtain effect included (curve 1) and for specular reflection (curve 3). Curve 2 is calculated for diffuse backscattering without the shower-curtain effect, and curve 4 is the case of pure single backscattering; $\lambda = 814$ nm, $\mu_s = 20\ \text{mm}^{-1}$, $g = 0.955$ ($\theta_{\text{rms}} = 0.3$ rad), $n = 1.4$, $f = 5$ mm, $w_0 = 0.5$ mm (From Ref. [10])

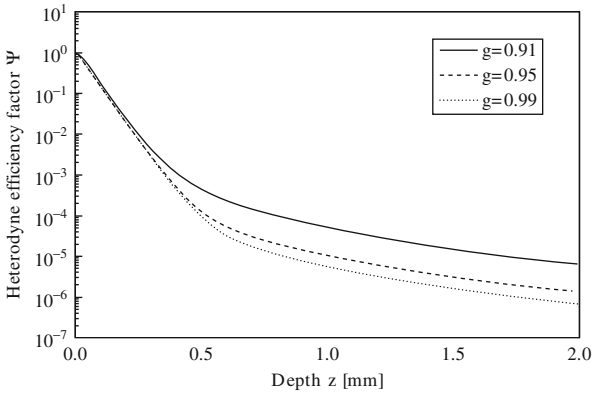

Fig. 17.3 $\Psi(z)$ as a function of z for $\mu_s = 10\ \text{mm}^{-1}$ and three values of g. The curves are for the case of a diffuse backscattering at the discontinuity and inclusion of the shower-curtain effect ($\lambda = 814$ nm, $n = 1.4$, $f = 5$ mm, $w_0 = 0.5$ mm)

slope occurs at different depths. This is due to the shower-curtain effect leading to an appreciable enhancement of $\Psi(z)$, and with it the heterodyne signal, which is obtained by comparing curves 1 and 2 in Fig. 17.2. Physically, this increase in the heterodyne signal is due to an enhanced spatial coherence of the multiple-scattered light.

In Fig. 17.3, $\Psi(z)$ is shown as a function of depth z for $\mu_s = 10\ \text{mm}^{-1}$ and three values of g within the range of validity of the EHF principle. The curves are computed for the case of diffuse backscattering at the discontinuity and inclusion of the shower-curtain effect. This figure demonstrates the degree of sensitivity of the heterodyne efficiency factor with respect to changes in the asymmetry parameter. Moreover, in Fig. 17.4, $\Psi(z)$ is shown as a function of depth z for $g = 0.95$ and three values of μ_s within the range of interest with respect to tissue [43]. The curves are computed for the case of diffuse backscattering at the discontinuity and inclusion of the shower-curtain effect. This figure demonstrates the degree of sensitivity of the heterodyne efficiency factor with respect to changes in the scattering coefficient.

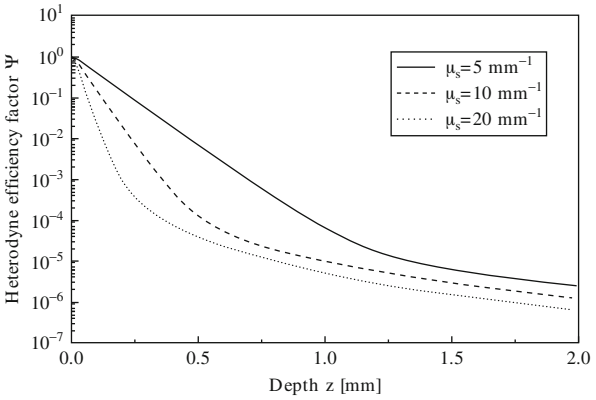

Fig. 17.4 $\Psi(z)$ as a function of z for $g = 0.95$ and three values of μ_s within a range of interest with respect to tissue. The curves are for the case of a diffuse backscattering at the discontinuity and inclusion of the shower-curtain effect ($\lambda = 814$ nm, $n = 1.4$, $f = 5$ mm, $w_0 = 0.5$ mm)

17.2.2.5 Choice of Scattering Function

In the present modeling of the OCT geometry, we use a Gaussian volume scattering function [19], as discussed in Sect. 17.2.3 below. The motivation for this choice of scattering function is the ability to obtain an accurate analytic engineering approximation, valid for all values of the optical depth. In the case of the Henyey-Greenstein scattering function [47], which is widely used in approximating the angular scattering dependence of single-scattering events in some biological media [43, 48], the corresponding analytic approximation is not as accurate as for the case of a Gaussian scattering function. However, a numerical computation using the exact expressions may be carried out instead. Hence, both scattering functions may be used in the modeling of the OCT geometry presented in this chapter.

17.2.2.6 Signal-to-Noise Ratio (SNR)

Without loss of generality, an OCT system with shot-noise-limited operation is considered in a calculation of the signal-to-noise ratio (SNR). The only significant source of noise is the shot-noise caused by the reference beam. For a photoconductive detector, the mean square noise power N_p can then be expressed as [49]

$$N_p = 2\alpha q_e G_{ca}^2 R_l B_w P_R, \tag{17.34}$$

where R_l is the resistance of the load, G_{ca} the gain associated with the current amplifier, and B_w the system bandwidth. The corresponding mean heterodyne signal power $S(z)$ is given by [50]

$$S(z) = \langle i^2(z) \rangle G_{ca}^2 R_l, \tag{17.35}$$

where $\langle i^2(z) \rangle$ is given by (17.27). Hence, the mean signal-to-noise ratio $SNR(z)$ is given by

$$SNR(z) = \frac{S(z)}{N_p} = (SNR)_0 \Psi(z), \tag{17.36}$$

where the signal-to-noise ratio in the absence of scattering $(SNR)_0$ is given by

$$(SNR)_0 = \frac{\eta P_S}{2h\nu B_w}\left(\frac{\sigma_b}{\pi w_H^2}\right). \tag{17.37}$$

In the case of interest where the focal plane coincides with the tissue discontinuity, we get the following expression for $(SNR)_0$

$$(SNR)_0 = \frac{2\eta P_S}{h\nu B_w}\left(\frac{w_0}{f}\right)^2 R_d, \tag{17.38}$$

where it has been used that $\sigma_b = 4\pi R_d/k^2$.

Calculation of the Maximum Probing Depth

The maximum probing depth is of considerable interest in the characterization and optimization of an OCT system when used for imaging in highly scattering tissue. The maximum probing depth may be calculated by using the model presented above. Details of the calculation are found in Ref. [27], where the calculation of the maximum probing depth z_{max} is based on the minimum acceptable *SNR* in the case of shot-noise-limited detection. In the calculations, a value of 3 is used as the minimum acceptable signal-to-noise ratio, that is, $SNR(z_{max}) = 3$.

An important conclusion of Ref. [27] is that, in general, z_{max} depends on the focal length at small values of the scattering coefficient but is independent of the focal length at larger values of the scattering coefficient. A similar behavior is observed for z_{max} as a function of μ_s and the $1/e$ intensity radius of the sample beam being focused. This behavior is due to multiple scattering of the light in the tissue. At scattering coefficients found in human skin tissue [43, 51], for example, it is concluded that the maximum probing depth is independent of the focal length f. This is an important conclusion because the depth of focus and the lateral resolution of the OCT system may then be chosen independently of z_{max}. For example, if no scanning of the focal plane in the tissue is desirable and, therefore, a large depth of focus has been chosen, the same maximum probing depth is obtained as for a system with a short depth of focus where the focal plane is scanned to keep it matched to the reference arm. This conclusion is not surprising or contrary to assumptions already held in the field. However, the theoretical analysis in this section provides a theoretical foundation for such statements. Moreover, this agreement may also be taken as a further validation of the OCT model presented here.

17.2.3 The OCT Lateral Resolution

As already discussed, the lateral resolution of an OCT system is determined by the spot size at the depth being probed in the tissue. Therefore, we determine the mean

irradiance distribution or the intensity pattern of the optical field as a function of the probing depth z in the tissue. In highly scattering tissue, the mean irradiance distribution, and with it the lateral resolution, is dependent on the scattering properties of the tissue. The formalism presented in this chapter enables the calculation of the lateral resolution in highly scattering tissue, which is shown below.

For small-angle scattering, where the paraxial approximation is valid, the EHF principle yields that the mean irradiance distribution is given by [40]

$$\langle I(r)\rangle = \left(\frac{k}{2\pi B}\right)^2 \int K(\rho)\exp\left\{\frac{ik}{B}\boldsymbol{\rho}\cdot\mathbf{r}\right\}\Gamma_{pt}(\rho)d^2\rho, \tag{17.39}$$

where

$$K(\rho) = \int \exp\left\{-\frac{ikA}{B}\boldsymbol{\rho}\cdot\mathbf{P}\right\}U_{Si}(\mathbf{P}+\boldsymbol{\rho}/2)U_{Si}^{*}(\mathbf{P}-\boldsymbol{\rho}/2)d^2P, \tag{17.40}$$

and $\boldsymbol{\rho} = \mathbf{p}_1 - \mathbf{p}_2$. For an OCT system focusing at a depth z in the tissue, $A = 1$ and $B = f$. The mutual coherence function Γ_{pt} can be expressed as [45]

$$\Gamma_{pt} = \langle \exp\{i[\phi(\mathbf{p}_1) - \phi(\mathbf{p}_2)]\}\rangle = \exp\{-s[1 - b_\phi(\rho)]\}, \tag{17.41}$$

where we have assumed that the phase ϕ is a normally distributed zero-mean random process. The quantity s is the phase variance, and $b_\phi(\rho)$ is the normalized phase autocorrelation function for a point source whose origin is at the probing depth z. It can be shown [52] that the phase variance $s = \mu_s z$, which is equal to the optical depth. The normalized phase autocorrelation function $b_\phi(\rho)$ is given by [45]

$$b_\phi(\rho) = \frac{\int_0^L dz' \int_0^\infty \sigma(\theta; z')J_0(kp_s\theta)\theta d\theta}{\int_0^L dz' \int_0^\infty \sigma(\theta; z')\theta d\theta}, \tag{17.42}$$

J_0 is the Bessel function of the first kind of order zero,

$$p_s = \frac{B_b(z')}{B_b}\rho, \tag{17.43}$$

where $B_b(z')$ is the B-matrix element for backpropagation from the probing depth z to a distance z' and $\sigma(\theta; z')$ is the volume scattering or phase function with θ being the scattering angle. For the OCT geometry, $B_b(z') = z'/n$ for $0 \le z' \le z$, $L = d + z$, and

$\sigma(\theta; z') = \sigma(\theta)$ for $0 \le z' \le z$, and zero otherwise. In this model, we use a Gaussian volume scattering function, which in the small-angle approximation is given by

$$\sigma(\theta) = \exp\left[-\theta^2/\theta_0^2\right], \tag{17.44}$$

where $g = \langle \cos\theta \rangle \approx 1 - \langle \theta^2 \rangle / 2$ and $\theta_0 = \langle \theta^2 \rangle^{1/2} \approx [2(1-g)]^{1/2}$. Substituting (17.43) and (17.44) into (17.42) and performing the indicated integrations yield the following equation for the normalized phase autocorrelation function

$$b_\phi(\rho) = \frac{\sqrt{\pi}}{2} \frac{\rho_\phi}{\rho} \operatorname{erf}\left(\rho \Big/ \rho_\phi\right), \tag{17.45}$$

where $\operatorname{erf}(\rho/\rho_\phi)$ denotes the error function and ρ_ϕ is the phase correlation length given by

$$\rho_\phi = \frac{\lambda}{\pi\sqrt{2(1-g)}} \left(1 + \frac{nd}{z}\right). \tag{17.46}$$

Hence, the mutual coherence function Γ_{pt} is given by (17.41) with $b_\phi(\rho)$ given by (17.45). Thus, for specific values of both s and g, the mutual coherence function is completely determined, and for a given value of the initial optical wave function U_{Si}, numerical results for the mean irradiance can be obtained directly from (17.39). Here, U_{Si} is given by (17.13), and we get the following equation for the mean irradiance distribution at the probing depth z in the tissue

$$\langle I(\mathbf{r}) \rangle = \frac{P_S}{2\pi (f/kw_0)^2} \int_0^\infty \exp\left\{-\frac{x^2}{4}\right\} x J_0(ux) \Gamma_{pt}(xw_0) dx, \tag{17.47}$$

where J_0 is the Bessel function of the first kind of order zero and

$$u = \frac{r}{f/kw_0} \tag{17.48}$$

is a normalized transverse coordinate.

As indicated above, numerical results can readily be obtained. However, it is useful to have an analytic approximation so that OCT system parameter studies can be performed. Examination of (17.41) reveals for large values of the optical depth that Γ_{pt} is nonzero for $s\{1 - b_\phi(\rho)\}$ less than the order unity, that is, for $b_\phi(\rho)$ near unity. Expanding $b_\phi(\rho)$ in powers of ρ and retaining the first two nonzero terms yields from (17.45) that $b_\phi(\rho) \approx 1 - \rho^2/3(\rho_\phi)^2$, from which it follows that

$$\Gamma_{pt} \approx \exp\left[-\rho^2/\rho_0^2\right], \quad s >> 1, \tag{17.49}$$

where $\rho_0 = \rho_\phi (3/s)^{1/2}$. We expect that the ballistic, that is, unscattered, component of the irradiance pattern is proportional to $e^{-\mu s z}$. Thus, we approximate the mutual coherence function as

$$\Gamma_{pt} \approx e^{-\mu_s z} + (1 - e^{-\mu_s z}) \exp\{-\rho^2/\rho_0^2\}. \tag{17.50}$$

Substituting (17.13) and (17.50) into (17.39) and performing the integration yield the following approximate expression for the mean irradiance distribution at the probing depth z in the tissue

$$\langle I(\mathbf{r}) \rangle \approx \frac{P_S}{\pi} \left[\frac{e^{-\mu_s z} \exp\{-r^2/w_H^2\}}{w_H^2} + \frac{(1 - e^{-\mu_s z}) \exp\{-r^2/w_S^2\}}{w_S^2} \right]. \tag{17.51}$$

The first term in the brackets on the right-hand side of (17.51) can be interpreted to represent the attenuated distribution obtained in the absence of the inhomogeneities, and the corresponding second term represents a broader halo resulting from scattering by the inhomogeneities. The quantities w_H and w_S are the $1/e$ irradiance radii in the absence and presence of scattering, respectively, given by

$$w_H^2 = w_0^2 \left(A - \frac{B}{f} \right)^2 + \left(\frac{B}{k w_0} \right)^2, \tag{17.52}$$

$$w_S^2 = w_0^2 \left(A - \frac{B}{f} \right)^2 + \left(\frac{B}{k w_0} \right)^2 + \left(\frac{2B}{k \rho_0} \right)^2. \tag{17.53}$$

For the OCT system, we have

$$w_H = \frac{f}{k w_0}, \tag{17.54}$$

$$w_S = \sqrt{w_H^2 + \left(\frac{2f}{k \rho_0} \right)^2}. \tag{17.55}$$

It is only in the very superficial layers of highly scattering tissue that it is possible to achieve diffraction-limited focusing. In this region, the lateral resolution is given by $2w_H$. At deeper probing depths, the lateral resolution is dependent on the scattering properties and given by $2w_S$. It is seen from (17.55) and (17.29) that the lateral resolution is degraded due to multiple scattering when the probing depth is increased. This is illustrated in Fig. 17.5, where the intensity pattern is shown as a function of the probing depth z in the tissue using (17.51). Finally, from (17.55) and (17.29), it is important to note that the shower-curtain effect leads to an increased lateral resolution.

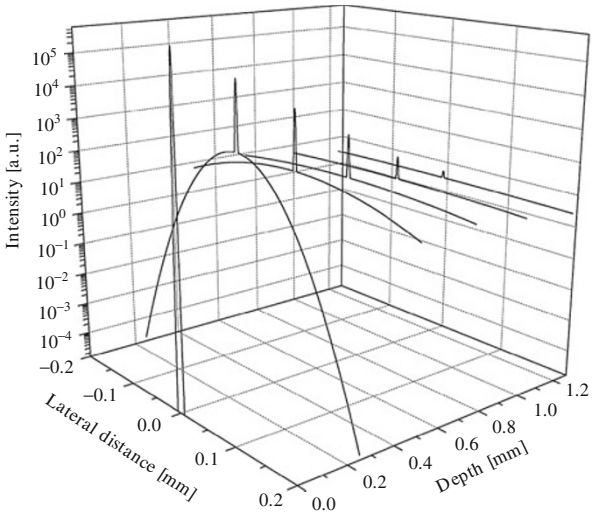

Fig. 17.5 The intensity pattern as a function of the probing depth z in the tissue ($\lambda = 814$ nm, $\mu_s = 10$ mm^{-1}, $g = 0.955$ ($\theta_{rms} = 0.3$ rad), $n = 1.4$, $f = 5$ mm, $w_0 = 0.5$ mm)

17.3 Advanced Monte Carlo Simulation of OCT Systems

In the previous section, the extended Huygens-Fresnel model was applied to model a generalized OCT setup, where the OCT signal from a diffusely reflecting discontinuity within the sample was found. In the following, we refer to this model as the EHF model. Also the so-called heterodyne efficiency factor Ψ was investigated, which describes the degradation of the OCT signal due to scattering. The predictions from the EHF model have been demonstrated to compare well with experiments carried out on aqueous suspensions of microspheres [10]. In this section, we describe the derivation of a Monte Carlo (MC) model of the OCT signal. As stated in the introduction, our motivation for applying MC simulation is to develop a model which may serve as a numerical phantom for further theoretical studies.

It is important to note that the MC method only describes the transport of energy packets along straight lines and therefore the approach is incapable of describing coherent interactions of light. These energy packets are often referred to as photon packets or simply photons, and this is adopted here. However, it should be emphasized that no underlying wave equation is guiding or governing these photons. Accordingly, any attempt to relate these to real quantum mechanical photons should be done with great care as argued in Ref. [53] regarding a suggested approach of including diffraction effects into MC simulations [54]. An MC photon packet represents a fraction of the total light energy, and for some applications, especially continuous wave, it may be useful to think of the path traveled by a photon as one possible path in which a fraction of the power flows. A collection of photon packets may then be perceived as constituting an intensity distribution due to an underlying field, and it can, accordingly, seem tempting to infer behavior

known to apply to fields upon photon packets. Consider, as an example, that one wishes to determine whether the photon packets are able to enter an optical fiber. It can then seem intuitively correct to restrict the access of photons impinging on the fiber end to those which fall within the numerical aperture of the fiber. However, such an angular restriction may not be correct, because the individual photon packet do not carry information of the entire field and its phase distribution. It is therefore not possible to determine whether a portion of the energy carried by a photon packet will enter the fiber due to a mode match between the fiber mode and the field underlying the collective intensity distribution of the photon packets. This discussion is treated in greater detail in Ref. [12].

With the above discussion of MC photons in mind, it may seem futile to investigate if MC simulation is applicable to estimate an OCT signal, which is the result of heterodyne mixing, and thus depends upon the coherence properties of the light. However, the problem may be reformulated to investigate whether or not the effect of the lack of coherence information in an MC simulation may be circumvented or at least minimized. Others [55–58] have attempted to model similar optical geometries by interpreting the heterodyne process as a rejection process in which the detected photons must conform to a set of criteria on position and angle. We refer to such a set of criteria as a detection scheme. However, these criteria were found by ad hoc considerations of the optical system, which may easily lead to incorrect results as exemplified above. Instead a mathematical derivation of the true criteria of the detection scheme will be given in this section.

In Sect. 17.3.1, the EHF principle is used to derive an expression for the OCT signal depending on the intensity of the light only. This is obtained by calculating the mixing of the reference and sample beams in the plane conjugate to the discontinuity plane in the sample probed by the system. The result is surprising, because the expression for the signal given in (17.9) depends on the coherence properties of the light. However, it is shown that the formula used for calculating the OCT signal in this particular plane is mathematically identical to the result in (17.9). These results are valid for the, from a biomedical point of view, important case of a signal arising from a diffusely reflecting discontinuity embedded in a scattering sample. As a novelty, this proves the viability of MC simulation to model the OCT technique, because it is shown that only intensity, and not field and phase, is necessary for this case. In Sect. 17.3.2, the necessary advanced method of simulating focused Gaussian beams in MC simulation is discussed. The results of Sects. 17.3.1 and 17.3.2 are then combined in Sect. 17.3.3 to form an MC model of the OCT signal. The results using this model are then compared to those of the EHF model in Sect. 17.3.4.

17.3.1 Theoretical Considerations

The optical geometry of the sample arm is shown in Fig. 17.6, and it should be noted that the enclosed section corresponds to the geometry used for the EHF calculation in Sect. 17.2.2. An optical fiber end is positioned in the *p*-plane.

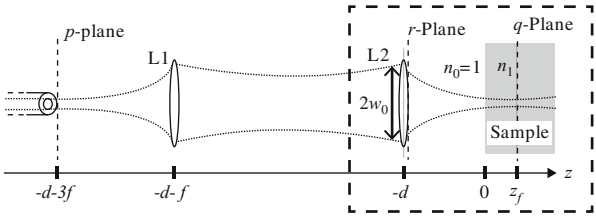

Fig. 17.6 Sample arm setup of the OCT system. The lenses L1 and L2 are considered to be identical, perfect, and have infinite radius. The setup is essentially a 4F system (From Ref. [12])

The fiber emits a beam, which hits the collimating lens L1. The focusing lens L2 is positioned in the *r*-plane, and in this plane, the beam is a Gaussian beam with $1/e$ width, w_0, of the intensity. The beam is focused by L2 upon a diffusely reflecting discontinuity positioned at the depth z_f inside a scattering sample a distance d from L2. The sample is taken to be a slab infinite in the transverse direction. The part of the light that is reflected from the discontinuity propagates out through the sample, through lenses L2 and L1 to the optical fiber, where it is collected. The lenses L1 and L2 have the focal length f and are taken to be identical, perfect, and infinite in radius. This means that the *q*- and *p*-planes are conjugate planes with magnification one.

The OCT signal is produced by the mixing of the light from the reference and sample arms on the photodetector of the OCT system. Due to the symmetry of the system, in Sect. 17.2.2, the EHF prediction of the mixing between signal and reference beam was conveniently calculated at the *r*-plane. The mean square of the signal current $\langle i^2 \rangle$ is given by (17.9) and rewritten according to the notation in Fig. 17.6 to yield

$$\langle i^2 \rangle = 2\alpha^2 |g(\tau)|^2 \,\mathrm{Re}\left[\iint \Gamma_R(\mathbf{r}_1, \mathbf{r}_2)\Gamma_S(\mathbf{r}_1, \mathbf{r}_2)\, d\mathbf{r}_1 d\mathbf{r}_2\right] \equiv \Psi_r \langle i_0^2 \rangle, \tag{17.56}$$

where $\Gamma_R(\mathbf{r}_1,\mathbf{r}_2) = U_R(\mathbf{r}_1)U_R{}^*(\mathbf{r}_2)$ is the cross correlation of the scalar reference field, $\Gamma_S(\mathbf{r}_1, \mathbf{r}_2) = \langle U_S(\mathbf{r}_1)U_S{}^*(\mathbf{r}_2)\rangle$ is the cross correlation of the sample field, and $\mathbf{r}_1$ and $\mathbf{r}_2$ are vectors in the *r*-plane (see Fig. 17.6). Ψ_r is the heterodyne efficiency factor (defined in (17.27); subscript *r* refers to it being calculated in the *r*-plane), which quantifies the reduction in signal due to scattering, and $\langle i_0{}^2 \rangle$ is the OCT signal current in the absence of scattering. The angle brackets denote an ensemble averaging over both the statistical properties of the scattering medium and the discontinuity, and the function $g(\tau)$ is the normalized temporal coherence function of the field, where τ is the time difference of propagation between the two fields.

It is important to note that by using the EHF principle, the investigation is limited to the paraxial regime as discussed above. In addition, most tissues are highly forward scattering in the near-infrared regime in which most OCT systems operate. It is assumed that the coherence length of the light source is short enough that signal powers from other reflections than the probed discontinuity are negligible. On the other hand, the coherence length is assumed long enough so that the temporal distortion of the sample field, or the path length distribution of the reflected photons, is assumed negligible compared to the coherence length of

the light source. Assuming that the optical path length of the reference beam and sample beam reflected from the discontinuity are perfectly matched, then $g(\tau) \approx 1$. To obtain the best comparison with the EHF model, the MC model presented in this section adopts this approximation.

The approximation of $g(\tau) \approx 1$ is a justified approximation for highly forward scattering tissues [8]. However, it does render the EHF model unsuitable to investigate the effect of scattering on the axial resolution of an OCT system in general, because the coherence gate due to the limited coherence length of the light source is not incorporated. Others have suggested using MC simulation and the total optical path length traveled by a photon packet to determine the influence of the coherence gate [9, 58, 59]. While this may very well be a valid approach, it is clear from the above discussion of photon packets and coherence that, how intuitively correct it may seem, this may not be the case. However, no efforts have been published to establish the meaning of a photon packet in such a temporal mixing of fields, so future work is required to establish such a relation. It is the intention that the MC model of the OCT signal presented in this chapter may be instrumental in such studies.

The OCT signal depends upon the lateral cross correlation of the light from the scattering sample (see (17.27)) and the lateral coherence length ρ_0 of the sample field in the r-plane for a single layer in front of the discontinuity is given by (17.29). With a nonzero lateral coherence length, ρ_0, it is seen that the OCT signal depends heavily upon the coherence properties of the field from the sample. As discussed above, an MC simulation does not describe the spatial coherence properties of light, and thus, a direct simulation of (17.56) is not possible. Like in Sect. 17.2.2, we assume that the discontinuity is diffusely reflecting and this infers that the lateral coherence will be zero immediately after reflection. Our motivation for envisioning the system geometry considered in Sect. 17.2.2 as part of a 4 F setup is to obtain a conjugate plane to the q-plane, here the p-plane (see Fig. 17.6). Through the conjugate relation, it is given that, in the absence of scattering, the lateral coherence length in the p-plane will also be zero. Hence, the sample field will be delta-correlated [19], and the OCT signal will only depend upon the intensities of the reference and sample field. In Appendix A, we show that within the paraxial regime, the sample field is delta-correlated even in the presence of scattering. We also show that the heterodyne efficiency factor calculated in the p-plane Ψ_p is mathematically identical to the heterodyne efficiency factor calculated in the r-plane, so that

$$\Psi_p = \frac{\langle i^2 \rangle}{\langle i_0^2 \rangle} = \frac{\int I_R(\mathbf{p}) \langle I_S(\mathbf{p}) \rangle d^2\mathbf{p}}{\int I_R(\mathbf{p}) \langle I_{S0}(\mathbf{p}) \rangle d^2\mathbf{p}} = \Psi_r, \tag{17.57}$$

where I_R is the intensity at the reference beam and I_S, I_{S0} are the received intensities of the sample beam with and without scattering, respectively. The quantity $\mathbf{p}$ is a vector in the p-plane (see Fig. 17.6). Equation (17.57) shows the viability of applying an MC simulation to an OCT system provided a good estimate of the intensity distribution of the sample field is achieved. This requires a method to

simulate a focused Gaussian beam, and a novel method for modeling such a beam using MC simulation is reviewed in Sect. 17.3.2. Note that the identity proven in (17.57) is only strictly valid within the approximations of the EHF principle and thus also within the paraxial regime. However, for geometries with scattering that is not highly forward directed, we expect coherence effects to be of even less importance, and thus, (17.57) should at least be a good first approximation even when the paraxial approximation is not strictly valid.

17.3.2 Modeling a Focused Gaussian Beam with Monte Carlo Simulation

Monte Carlo models have previously been applied to model the focusing of light beams in tissue. The motivations have been to study the distribution of absorbed power for photodynamic therapy (PDT) [60], the performance of confocal microscopy [55, 56, 59], the efficiency of 1- and 2-photon excitation microscopy [57, 61], OCT [9], and the distribution within turbid media in general [60, 62]. In the absence of scattering, the focusing behavior of the beam is simply determined from the initial coordinates and propagation angles of the photons being launched. By carrying out MC simulations, one may then determine the distortion caused by scattering and other structures. Previously, two different ways of modeling the focusing have been employed:

Geometric-focus method: The initial position of the photon launch is found stochastically according to the initial intensity distribution, and the photon packets are simply directed toward the geometric focus of the beam [9, 60, 62, 63]. The geometric-focus method is obviously only a good approximation to a Gaussian beam for a very hard focus, but even then, the infinite photon density of the unscattered photons at the geometric focus may pose a problem.

Spot-focus method: After the initial position has been found as in the geometric-focus method, the photon packets are then directed toward a random position within an area in the focal plane of the beam [55–57]. The position within the chosen spot in the focal plane may be chosen according to different probability distributions. If future applications of the proposed MC model involve the use of the path lengths of the received photon packets to study the effect temporal distortion of the light due to scattering, the stochastic nature of the photon paths may pose a problem.

We have developed a method of choosing initial coordinates and angles for the photons so that the full 3D spatial intensity distribution of a Gaussian beam, that is, both the correct beam waist and finite spot size at focus, is obtained. This may be realized by utilizing the hyperbolic nature of a Gaussian beam, and we denote this approach the *hyperboloid method*. It is important to notice that this method does not require more simulation time than the two methods discussed above. Moreover, since the photons are still launched along straight lines, the incorporation of the scheme into most MC simulation programs for light propagation will be straightforward. Details of the hyperboloid method may be found in Ref. [12].

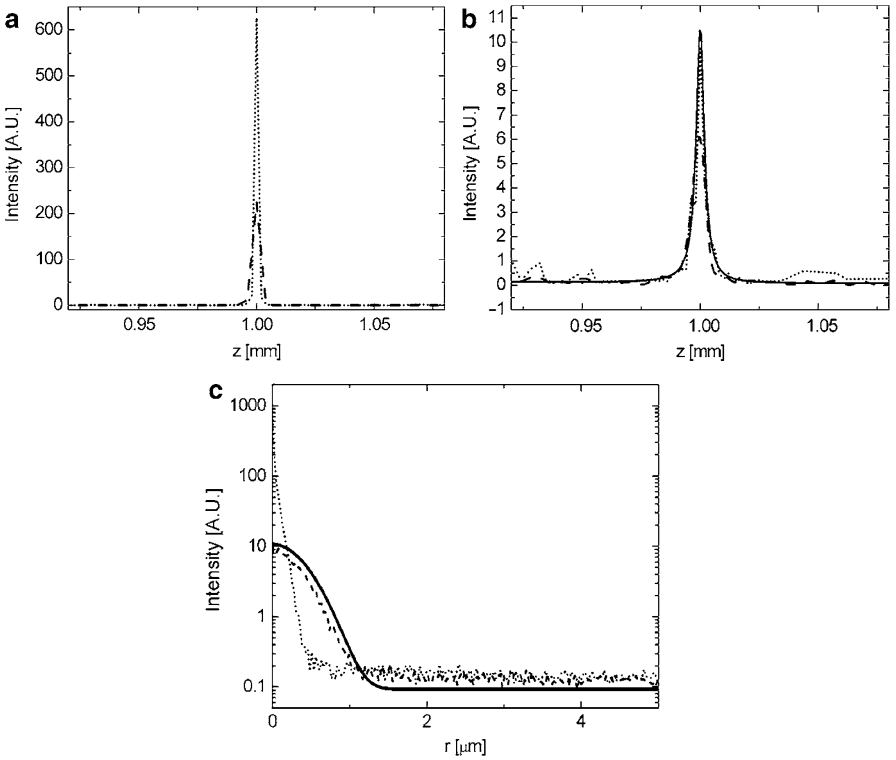

Fig. 17.7 The axial focus of a beam described in the text. All distributions have been normalized to unity for $(r, z) = (0, 0)$. (**a**) The axial intensity estimated using the geometric-focus method. *Dashed* curve is obtained with the *larger grid* and *dotted* curve with the smaller grid (see text). (**b**) Similar curves obtained with the hyperboloid method. The *solid* curve is the intensity distribution obtained from the integral expression (17.39). (**c**) The transverse intensity distribution (*small grid*) in the focal plane: *dotted* curve: the geometric-focus method; *dashed* curve: hyperboloid method; *solid* curve: the integral expression

As an illustration of the performance of the hyperboloid method, the intensity distribution of a collimated beam has been found using three different methods: MC with the hyperboloid method, MC with the geometric-focus method (the most commonly used method in the literature), and an integral expression (see (17.39)). The intensity distributions found using each method are shown in Fig. 17.7. The modeled beam is a collimated beam with $1/e$ intensity radius $w_0 = 0.4$ mm, which is focused by a lens with $f = 4.0$ mm at a depth of 1.0 mm into a scattering medium with $\mu_s = 10\ \text{mm}^{-1}$ and $g = 0.92$. The light propagation has been simulated using $50{\cdot}10^9$ photons for two sizes of the spatial discretization grid, $\Delta z = 4$ μm, $\Delta q = 0.5$ nm, and $\Delta z = 2$ μm, $\Delta q = 0.25$ nm. The resulting intensity distributions have all been normalized to unity at $(q,z) = (0,0)$.

In Fig. 17.7a and b, the axial intensity distributions predicted by the geometric-focus and the hyperboloid method are shown, respectively. The dotted curves are

the results of using the small grid size, whereas the dashed curves are the results of using the larger grid size. The solid curve in Fig. 17.7b is the result found by using integral expression in (17.39). For the large grid size, the geometric-focus method overestimates the peak height relative to the integral expression with a factor of 14, whereas the hyperboloid method underestimates the peak height with a factor of 0.5. We see that when the resolution is increased, the hyperboloid method approaches the result of the integral expression in (17.39) to a factor of 0.95, whereas the peak height estimated by the geometric-focus method increases even further to a factor of 41. The latter is a result of the infinite photon density of the unscattered photons in the geometric-focus method. It is noted that the high-resolution curve for the hyperboloid method (dotted curve in Fig. 17.7b) seems noisier than its counterpart from the geometric-focus method (dotted curve in Fig. 17.7a). In fact, the variance of the data used for the two curves is practically identical but less noticeable in Fig. 17.7a due to the scale necessary to show the peak intensity estimated by the geometric-focus method. In Fig. 17.7c, the transverse intensity distribution in the focal plane estimated by the geometric-focus method (dotted), the hyperboloid method (dashed), and the integral expression (solid) are plotted, respectively. From Fig. 17.7a and c, we see that the geometric-focus method is an inappropriate method for estimating the detailed intensity distribution around the focus. Figure 17.7b and c show an excellent agreement between the hyperboloid method and the integral expression. Thus, for modeling applications, where spatial resolution is important, as in OCT, the hyperboloid method should be used when doing MC simulation of focused Gaussian beam.

17.3.3 Monte Carlo Simulation of the OCT Signal

In Sect. 17.3.1, we found that the heterodyne efficiency factor of the OCT signal may be found using the knowledge of the intensity distributions of the sample and reference fields in the p-plane (see Fig. 17.6), where the fiber end is situated:

$$\Psi_p = \frac{\int I_R(\mathbf{p})\langle I_S(\mathbf{p})\rangle d^2\mathbf{p}}{\int I_R(\mathbf{p})\langle I_{S0}(\mathbf{p})\rangle d^2\mathbf{p}}. \tag{17.58}$$

In the EHF principle, the effect of a scattering medium is treated as a random phase distortion added to the deterministic phase of the light as it propagates through the medium. In the derivation of (17.58) (see Sect. 17.7), it is necessary to assume that the phase distortion added to the light propagating toward the discontinuity is statistically independent from the phase distortion added to the light propagating away from the discontinuity. It is important to note that this assumption is inherently fulfilled by MC methods such as that used by the MCML computer code [64]: A photon is traced through a dynamic medium in the sense that the distance to the next scattering event and scattering angle is a random variable independent upon the past of the photon. Hence, after each

stochastic event, the photon experiences a different realization of the sample. Therefore, an ensemble averaging over the stochastic sample in (17.58) is carried out through a single simulation. Moreover, to also obtain an averaging in the modeling of the diffusely reflecting discontinuity, each reflected photon must experience a new realization of the discontinuity. Thus, we use the macroscopic intensity distribution of a Lambertian emitter [19] to sample the reflected angle:

$$I_r(\theta_r) = I_T \cos\theta_r. \tag{17.59}$$

Here, I_T is the reflected intensity at $\theta_r = 0$ and θ_r is the reflected angle. By following the method outlined by Prahl et al. [65] of sampling a physical quantity using a computer-generated pseudorandom, we obtain the relations

$$\theta_r = \arcsin(\xi), \tag{17.60}$$

$$\varphi_r = 2\pi\zeta, \tag{17.61}$$

where φ_r is the azimuthal angle of the reflected photon and ξ and ζ are both random numbers evenly distributed between 0 and 1.

Accordingly, the method of simulating the OCT signal is carried out as follows. The MC photon packet is launched from the focusing lens in the r-plane (see Fig. 17.6) using the new hyperboloid method described in Sect. 17.3.2. The interfacing with specular surfaces, such as the sample surface and the propagation through the scattering medium, is carried out using the MCML computer code. When a photon packet is reflected off the diffusely reflecting discontinuity, (17.60) and (17.61) are used to determine the direction of the photon after reflection. As a photon exits the sample after interaction with the discontinuity, its position and angle is used to calculate its position in the p-plane after propagation through the 4F system. To evaluate (17.58), numerically consider that the m'th photon packet exiting the medium contributes to the intensity at the point p_m in the p-plane by the amount

$$I_{S,m} \propto \frac{w_m}{\Delta p^2}, \tag{17.62}$$

where w_m is the energy, or weight, carried by the photon packet and Δp^2 is a differential area around p_m. Using this and (17.58), the MC estimated heterodyne efficiency factor Ψ_{MC} is then given by

$$\Psi_{\mathrm{MC}} = \frac{\sum_m^M I_R(p_m) I_{S,m} \Delta p^2}{\langle i_0^2 \rangle} = \frac{\sum_m^M I_R(p_m) \mathrm{w}_m}{\langle i_0^2 \rangle}, \tag{17.63}$$

where $I_R(p)$ is the intensity distribution of the reference beam in the p-plane, and it is noted that the reference beam has a Gaussian intensity distribution of width w_f

in the p-plane. The signal in the absence of scattering $\langle i_0^2 \rangle$ may be either simulated or calculated. The latter is straightforward, because with the conjugate relationship between the p- and q-plane, the intensity distribution of the sample beam will be identical to that of the reference beam in the absence of scattering.

Equation (17.63) reveals the important detection criterion of the MC simulation of the OCT signal: a photon must hit the p-plane within the extent of the reference beam. While detection schemes of previously published MC models of OCT also incorporate that photons must hit the detector, the novelty of this detection scheme is the analytically derived size and necessary position in the p-plane. Furthermore, contrary to these schemes, the model does not incorporate an angular criterion that a photon packet must fulfill in order to contribute to the signal. It may seem counterintuitive that photon packets contribute to the desired signal without penalty regardless of angle of incidence upon the fiber in the p-plane. However, as demonstrated in Ref. [12], the inclusion of an angular criterion related to the angular extent of the incident beam, or equivalently the numerical aperture of the fiber, yields incorrect results.

17.3.4 Numerical Validation

17.3.4.1 Beam Geometries for Numerical Comparison

A set of beam geometries has been selected for numerical comparison between the EHF model and the MC model. These geometries are selected so that the two approaches are compared for different degrees of focusing and distances between the lens L2 and the sample. The selected cases are listed in Table 17.1 and are referred to as cases 1 through 4, respectively.

For all cases, the mean refractive index of the sample before the discontinuity and the surroundings are assumed to be matched so that $n_0 = n_1 = 1$. We wish to investigate the effect of scattering on the OCT signal. A difference in the refractive index between the sample and the surrounding will impose a Snell's law refraction at the interface, which in turn imposes a focus distortion not treated in the paraxial approximation ($\sin\theta \approx \theta$) and thus not described by the EHF model. Such a distortion will be difficult to separate from the effects of scattering and is thus omitted here. As discussed in Ref. [62], there is only a severe distortion for very tightly focused beams.

In all cases discussed in the following, the wavelength of the light is chosen to be 814 nm, which is one relevant wavelength for biomedical applications of OCT. The sample is assumed to exhibit scattering described by a Gaussian scattering function (see, e.g., Chap. 13 in Ref. [32]). The motivation for this choice is to enable comparison to analytical models of the propagation of Gaussian beams in random media [40] and the OCT signal (see Sect. 17.2.2), which both apply the Gaussian scattering function. The comparisons presented here are carried out for different degrees of scattering and for two relevant values of the asymmetry parameter in tissue [43]: very highly forward scattering ($g = 0.99$)

Table 17.1 Beam geometries for the four cases

Case number	f [mm]	d [mm]	z [mm]	w_0 [mm]	w_0/f
1	16.0	15.5	0.5	0.125	0.008
2	8	7.5	0.5	0.4	0.05
3	0.5	0.0	0.5	0.125	0.25
4	16.0	15.0	1.0	4	0.25

and highly forward scattering ($g = 0.92$). The value $g = 0.92$ was the value of the asymmetry factor in the experiments performed to validate the EHF model by Thrane et al. [10] With these two cases, the two approaches are compared for a sample geometry where the paraxial approximation is well satisfied and for a sample geometry, which is close to the limit of the paraxial approximation. Accordingly, it is expected that the best agreement will be found for $g = 0.99$.

Comparison

In Fig. 17.8, Ψ is plotted for cases 1 through 4 as a function of the scattering coefficient μ_s, and for reference, the case of single backscattering, that is, $\Psi_{\text{single}} = \exp(-2\mu_s z)$, has been included.

Three important observations may be made from Fig. 17.8. Firstly, we observe fine agreement between the MC method and the EHF model for the four cases tested. Thus, we consider these plots as validation of the MC model. Secondly, it is inferred that the OCT signal for high optical depths is a result of multiple-scattering effects in agreement with Sect. 17.2.2. This is seen by comparing the single-scattering curve to the plots of the MC and EHF. Finally, an important result of Sect. 17.2.2 was the inclusion of the so-called shower-curtain effect [29]. It is an effect caused by multiple scattering and thus plays an important role in calculating the OCT signal as the optical depth increases. Omitting this effect leads to an underestimation of the OCT signal of several orders of magnitude. Due to the fine agreement between the EHF model (with the shower-curtain effect included) and the MC model, we obtain the important result that the MC model inherently takes the effect into account.

For cases where the approximation of the EHF model is well satisfied, we attribute the observed deviation between the EHF and MC models to be caused by coherence effects in the intensity distribution of the sample field. Apparently, from Fig. 17.8, the lack of coherence information leads to an underestimation of Ψ, but the specific cause for this has yet to be determined. Ψ is by definition unity in the absence of scattering, and for large optical depths, coherence effects are expected to be negligible. Accordingly, we expect the two models to agree for small and large values of the optical depth of the discontinuity, whereas some deviation is to be expected in the intermediate region. As a highly forward scattering event perturbs the field only to a small degree, it is expected to distort coherence effects less than a more isotropic scattering case. In order to plot the relative deviation as a function of the effective distortion of the coherence, we plot the

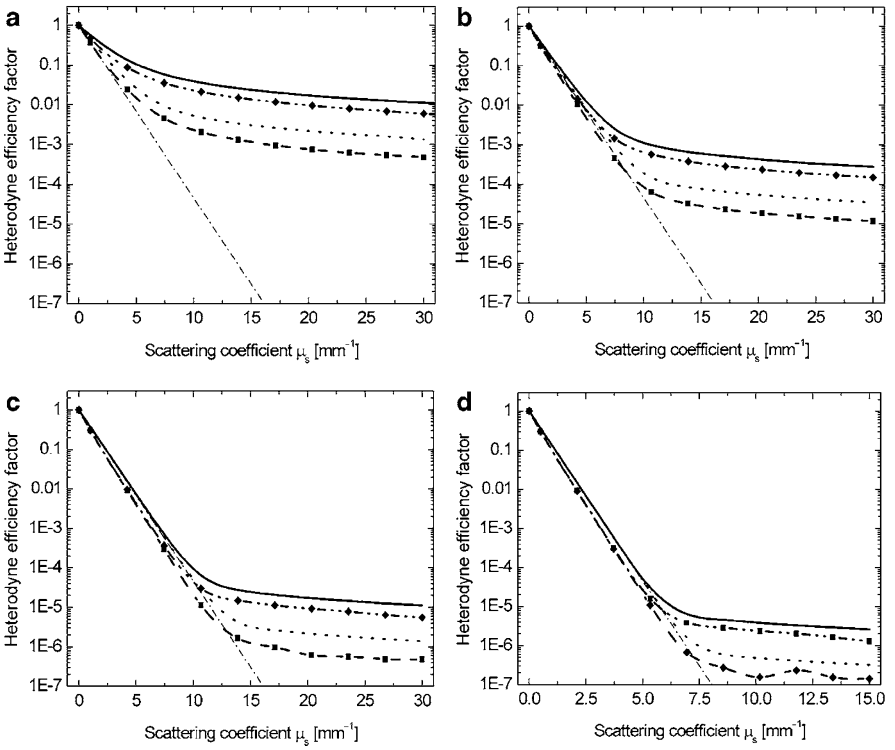

Fig. 17.8 Heterodyne efficiency factors estimated using, respectively, the EHF model and the MC method for two cases of g. (**a**), (**b**), (**c**), and (**d**) show the estimated values for geometries 1, 2, 3, and 4 in Table 17.1, respectively. The *solid line* and *dotted line* curves are the results of the EHF model for $g = 0.99$ and $g = 0.92$, respectively. *Dash-dot-dot* and *dashed curves* are the results of the MC simulations for $g = 0.99$ and $g = 0.92$, respectively. Diamonds (♦) and squares (■) mark the actual data points obtained by the MC simulation method. For comparison, the exponential reduction in signal due to scattering obtained by a single-scatter model is shown as a *dash-dot* curve

ratio $\Psi_{\mathrm{EHF}}/\Psi_{\mathrm{MC}}$ as a function of the transport reduced optical depth of the discontinuity given by

$$S_{tr} = \mu_z Z_f (1 - g). \tag{17.64}$$

The relative difference between the EHF model and the MC method behaves, qualitatively, identical as a function of s_{tr} independent of beam geometry and g. This is illustrated in Fig. 17.9 for cases 2 ($g = 0.92$ and 0.99), 3 ($g = 0.92$), and 4 ($g = 0.92$), respectively. The difference between the two approaches increases as a function of s_{tr} until $s_{tr} \approx 0.5$ after which it evens out. We mainly attribute this to the coherence effects in the intensity distribution discussed above. The more abrupt behavior of the curve for geometry 4 is attributed to a higher numerical uncertainty

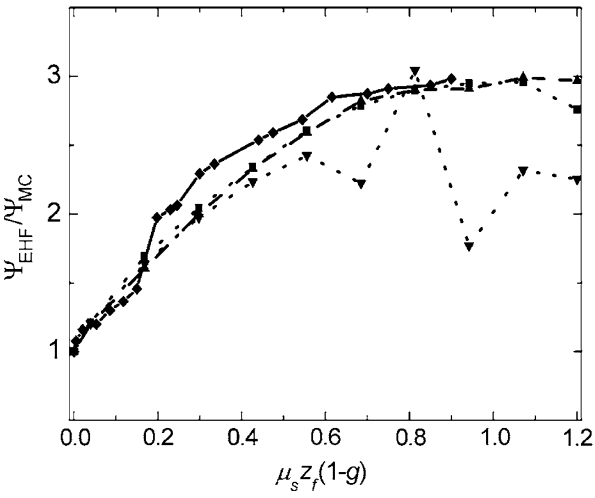

Fig. 17.9 The relative numerical difference between the results of the EHF model and the MC model from Fig. 17.8 for a representative selection of the considered geometries. The ratio Ψ_{EHF}/Ψ_{MC} is plotted for case 2 and $g = 0.99$ with symbols (♦) and *solid* curve, for case 2 and $g = 0.92$ with symbols (■) and *dash-dot-dot* curve, for case 3 and $g = 0.92$ with symbols (▼) and *dashed* curve, and for case 4 and $g = 0.92$ with symbols (●) and *dotted* curve (From Ref. [12])

in the case, caused by a more tightly focused beam. According to the new detection scheme, this implies that fewer photons will contribute to the signal resulting in an increased variance.

In summary, due to the fine agreement between the results of the EHF model and MC simulations borne out in Figs. 17.8 and 17.9, we conclude that the MC simulation presented in this section is a viable method of simulating the heterodyne efficiency factor of an OCT signal.

17.4 True-Reflection OCT Imaging

The interpretation of conventional OCT images may be a difficult task. One reason for this is the fact that an OCT signal, measured at a given position in a non-absorbing scattering medium, is a result of not only the amount of light reflected at the given position but also the attenuation due to scattering when the light propagates through the scattering medium. Therefore, to make images, which give a direct measure of the amount of light reflected at a given position, thereby making interpretation of OCT images easier, it is necessary to be able to separate reflection and scattering effects.

In this section, we present the concept of a so-called true-reflection OCT imaging algorithm [46] based on the analytical model described in Sect. 17.2. With this algorithm, it is possible to remove the effects of scattering from conventional OCT images and create so-called true-reflection OCT images. This kind of post-processing is similar to the correction for attenuation well known in ultrasonic imaging. In that field, a mathematical model describing the relationship between the received signal and the two main acoustic parameters, backscatter and attenuation, has been considered [66]. The model has then been used to guide the derivation of a processing technique with the aim of obtaining ultrasonic images that faithfully represents one acoustic parameter, such as backscatter [66]. Due to the similarity

between the ultrasonic case and the situation encountered in OCT, this forms a strong basis for introducing the concept of a true-reflection OCT imaging algorithm. The principle of the true-reflection OCT imaging algorithm is demonstrated experimentally by measurements on a solid scattering phantom in Sects. 17.4.2 and 17.4.3 on a heterogeneous sample simulated by using the MC model presented in Sect. 17.3.

17.4.1 True-Reflection OCT Imaging Algorithm

It was shown in Sect. 17.2.2 that the mean square heterodyne signal current for light reflected at depth z in the tissue may be expressed as $\langle i^2(z)\rangle = \langle i^2(z)\rangle_0 \Psi(z)$, where $\langle i^2(z)\rangle_0$ is the mean square heterodyne signal current in the absence of scattering and $\Psi(z)$ is the heterodyne efficiency factor, which includes all of the scattering effects. The maximum of the envelope of the measured interference signal corresponds to $\left[\langle i^2(z)\rangle\right]^{1/2}$. Thus, by dividing the envelope of the measured interference signal with $[\Psi(z)]^{1/2}$, we are able to correct for the scattering effects, that is, compensate for attenuation, and determine the envelope that would be obtained in the absence of scattering. It is important to note that in addition to the system parameters λ, f, and w_0, knowledge about μ_s, θ_{rms}, and n of the scattering medium is necessary in order to enable calculation of $[\Psi(z)]^{1/2}$. However, in practice, μ_s and θ_{rms} may be obtained by fitting the expression for $\left[\langle i^2(z)\rangle\right]^{1/2}$ to a measured depth scan of the homogeneous backscattering tissue using an estimated value of n and the appropriate system parameters. Implementing this procedure as an option in the imaging program provides the opportunity to make what may be labeled *true-reflection OCT images*.

17.4.2 Experimental Demonstration of the True-Reflection OCT Imaging Algorithm

The principle of the true-reflection OCT imaging algorithm is demonstrated experimentally by measurements on a solid scattering phantom using a conventional OCT system comprised by a superluminescent diode with a center wavelength of 814 nm (22.8 nm spectral bandwidth (FWHM), 1.9 mW output power), a fiber-optic Michelson interferometer with movable reference mirror, and a silicon photodetector. The two system parameters f and w_0 are 16 mm and 0.125 mm, respectively [67].

The solid phantom having three discontinuities, A, B, and C, with identical reflection coefficients, is shown in Fig. 17.10. It consists of scattering microspheres (approximate diameter size 10 μm) in a polymer. The optical parameters of the solid phantom, that is, the asymmetry parameter, the scattering coefficient, and the absorption coefficient, were determined by carrying out integrating sphere and collimated transmission measurements and using the inverse adding-doubling method [68]. It turned out that the phantom had negligible absorption.

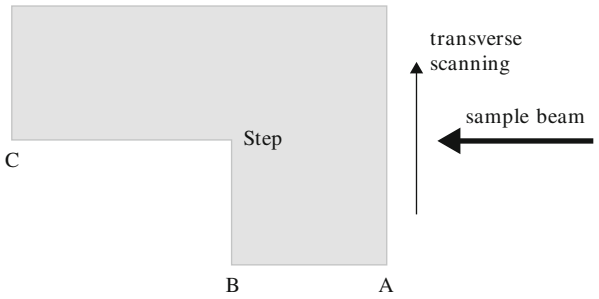

Fig. 17.10 A schematic of the solid phantom used in the demonstration of the true-reflection OCT imaging algorithm

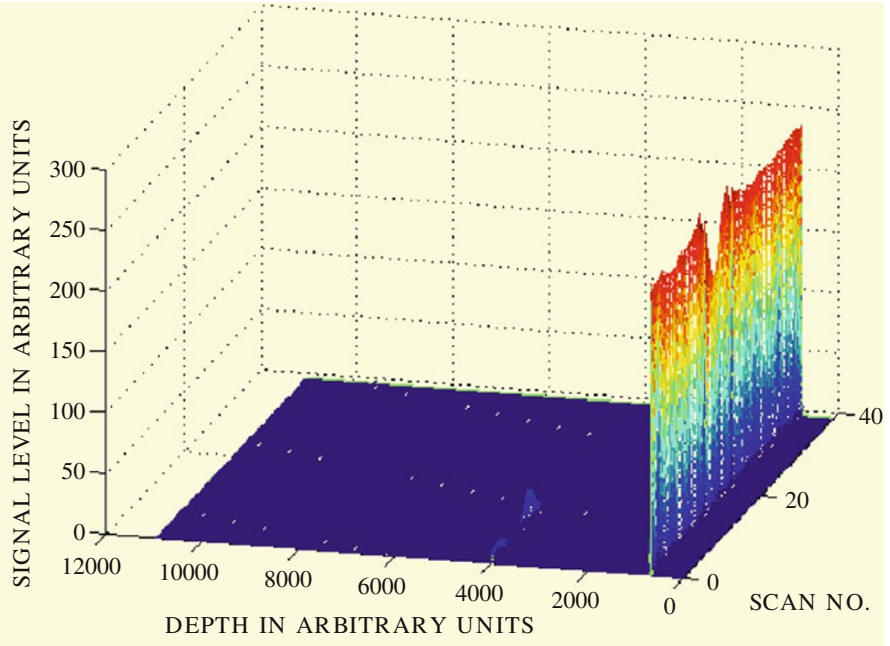

Fig. 17.11 The original unprocessed envelopes of the 40 longitudinal scans (From Ref. [67])

In the experiment, 40 longitudinal (horizontal) scans are performed across the step as indicated in Fig. 17.10. The distance between adjacent longitudinal scans is 10 μm, and only one longitudinal scan is taken in every lateral position. The light is reflected at the air-phantom discontinuity A ($z = 0.0$ mm) and at the two phantom-air discontinuities at $z = 2.0$ mm (B) and $z = 5.2$ mm (C), respectively, which all give a diffuse backscattering. The backscattering from the bulk of the phantom is negligible and cannot be detected.

The original unprocessed envelopes of the 40 longitudinal scans are shown in Fig. 17.11 with the use of a linear palette. The orientation is similar to the

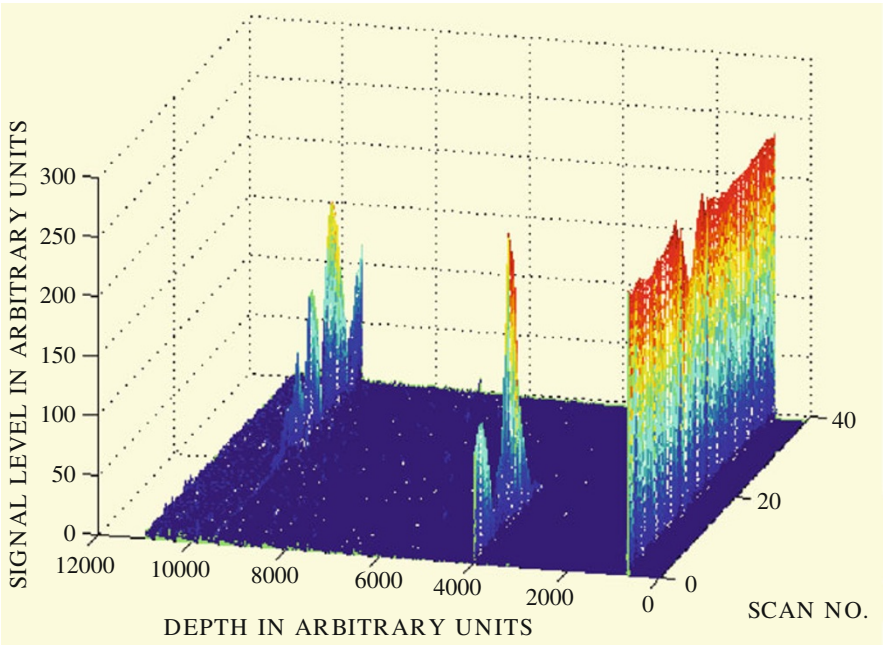

Fig. 17.12 The result of using the true-reflection OCT imaging algorithm on an OCT image of a solid phantom having three discontinuities (pos. A, B, and C) with identical values of their reflection coefficients (From Ref. [67])

orientation in Fig. 17.10. For a better visualization of the effect of the true-reflection OCT imaging algorithm, the envelopes are shown as a 3D plot. The first signal from the right is due to light reflected at the air-phantom discontinuity A, which will be denoted *the first discontinuity* in the following. The signal from the phantom-air discontinuity B at $z = 2.0$ mm (*the second discontinuity*) and the signal from the phantom-air discontinuity C at $z = 5.2$ mm (*the third discontinuity*) cannot be distinguished in Fig. 17.11. This is due to the scattering of the light in the phantom, which attenuates the signal.

By using the true-reflection OCT imaging algorithm described above to correct for the scattering effects, we get the envelopes shown in Fig. 17.12. The optical parameters of the solid phantom, which were used in the algorithm, are $\mu_s = 1.815\ \text{mm}^{-1}$, $\theta_{rms} = 0.1096$ rad ($g = 0.994$), and $n = 1.5$. As expected, the three signals from the discontinuities A, B, and C are nearly equal in strength after using the algorithm. A plausible explanation of the lateral variations of the signal is speckle [19], which is a well-known effect in OCT [69]. In addition, variation of the signal close to the step (see Fig. 17.10) is likely due to a partly reflection of the beam.

The experimental errors of the measured values of μ_s and g of the solid phantom have been estimated to be ± 5 % and ± 1 %, respectively. Values of μ_s +5 % and -5 % have been used in the algorithm, but the changes of the signal levels were

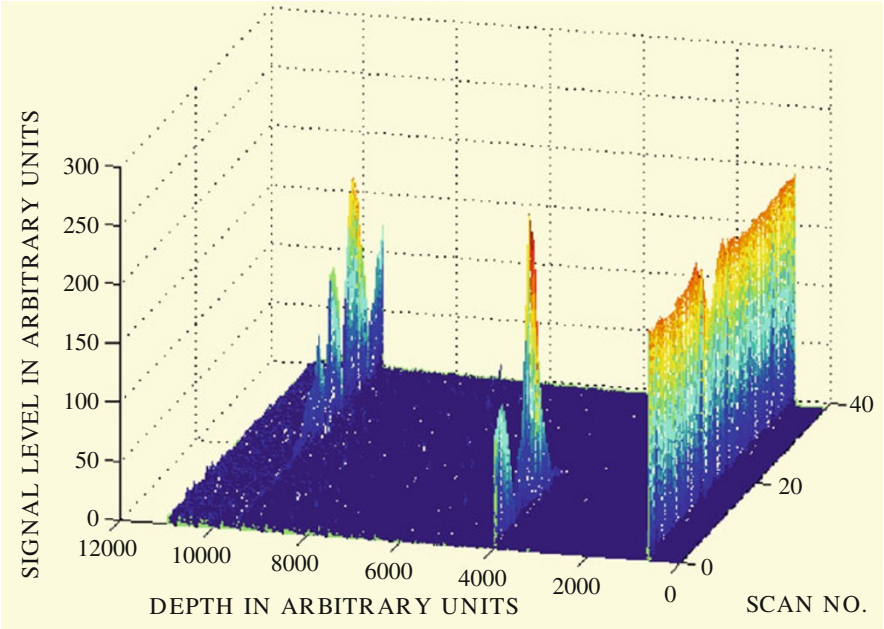

Fig. 17.13 The envelopes of the 40 longitudinal scans when the true-reflection OCT imaging algorithm has been used together with a value of $g - 1$ % (From Ref. [67])

very small. This is in contrast to the observation when a value of $g - 1$ % was used in the algorithm, and the envelopes are shown in Fig. 17.13. Note that the maximum signal of the second discontinuity is now slightly larger than the signal from the first discontinuity. However, the maximum signal levels of the second and third discontinuities seem to be closer to the signal level of the first discontinuity as compared to Fig. 17.12.

Figure 17.14 shows, for comparison, the envelopes obtained if only the single-scattering term is used in the expression for Ψ. Due to a large overestimate of the signal from the third discontinuity in this case, the signals from the first and second discontinuities are too small in amplitude to be observed in Fig. 17.14. Thus, it is obvious that the single-backscattering model is not sufficient, and furthermore, it demonstrates the importance of taking multiple-scattering effects into account.

The experiment demonstrates the feasibility of the new algorithm for a homogeneously scattering medium. However, the algorithm may be extended to cover heterogeneously scattering media, for example, skin tissue. *True-reflection OCT images* may be easier to interpret than conventional OCT images, and improved diagnosis may be envisioned due to a better differentiation of different tissue types.

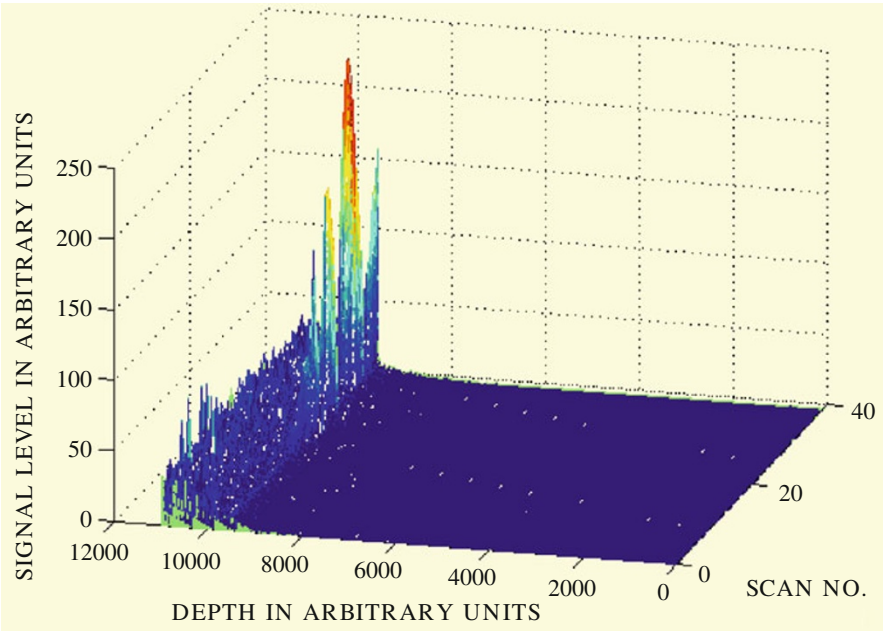

Fig. 17.14 The envelopes obtained by using the true-reflection OCT imaging algorithm when only the single-scattering term is used in the expression for Ψ (From Ref. [67])

17.4.3 True-Reflection OCT Imaging on an MC-Simulated Heterogeneous Multilayered Sample

The MC model presented in Sect. 17.3 may be used as a numerical phantom, which, for example, could be used to investigate the performance of the EHF model for sample geometries difficult to produce in the laboratory or for which one or more of the approximations made in the EHF model do not hold. It is important to note that the predictions from the EHF model have been demonstrated to compare well with experiments carried out on single-layered phantoms consisting of aqueous suspensions of microspheres [10]. In this section, we demonstrate the true-reflection OCT imaging algorithm on a heterogeneous multilayered sample using the MC model following the outline in Ref. [70].

Multilayered structures are at best difficult to manufacture, and the simulation of such structures using the MCML computer code is well established. Thus, we use the MC model to simulate the OCT signal for a two-layer sample in order to demonstrate the true-reflection OCT imaging algorithm on a heterogeneous sample. Through the incorporation of the ABCD matrix formalism in the EHF theory, it is straightforward to model the OCT system applied to a multilayered sample (see Appendix A of Ref. [10]). Thus, to demonstrate the true-reflection algorithm, we fit the two-layer EHF expression for the OCT signal to the MC simulation,

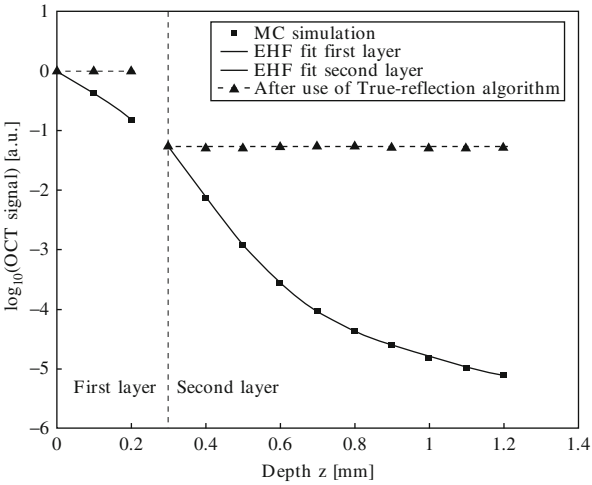

Fig. 17.15 MC simulation of the OCT signal for a two-layer sample (*squares*); EHF fit to the first and second layers (*solid line*); the MC simulation of the OCT signal after use of the true-reflection algorithm (*triangles* connected with a *dashed line*) (From Ref. [70])

Table 17.2 The input parameters of the MC simulation, together with the extracted parameters obtained by using the EHF model, and the percentage difference

Layer no.	Input μ_s [mm^{-1}]	Fitted μ_s [mm^{-1}]	Difference [%]	Input g	Fitted g	Difference [%]
1	5.00	4.92	−1.6	0.9900	0.9834	−0.67
2	10.00	10.22	2.2	0.9200	0.8586	−6.67

extract the optical properties of the two layers, and use these values of the optical properties in the algorithm to correct for the attenuation caused by scattering.

As in the previous MC simulations in Sect. 17.3, the refractive indices of the sample and the surroundings are matched and equal to unity. The system parameters in this case are $\lambda = 800$ nm, $w_0 = 0.4$ mm, and $f = 8.0$ mm. The first layer is 0.3 mm thick and has a constant scattering coefficient of $\mu_{s1} = 5.0$ mm^{-1} and $g_1 = 0.99$. The second layer is 0.9 mm thick and has a constant scattering coefficient of $\mu_{s2} = 10.0$ mm^{-1} and $g_2 = 0.92$. The MC simulation of the mean square heterodyne signal current is shown as squares in Fig. 17.15. The fit of the two-layer EHF model to the MC simulation is shown as a solid line in Fig. 17.15, and the hereby extracted optical properties μ_s and g (n is not a fitting parameter) of the two layers are shown in Table 17.2 together with the input parameters of the MC simulation. The relatively large point separation of the MC simulation in the z-direction makes the gap between the last point of the first layer and the first point of the second layer rather distinct in this case.

The small percentage difference shown in Table 17.2 between the MC input parameters and the extracted parameters demonstrates the capability of the EHF model to extract optical properties from a heterogeneous multilayered sample, for example, human skin. The extracted optical properties of the two layers may now be used in the true-reflection algorithm. Thus, the MC simulation of the OCT signal

after use of the true-reflection algorithm, that is, after correction for the attenuation caused by scattering, is shown as triangles in Fig. 17.15 connected by a dashed line. The distinct signal levels obtained for the two different layers after using the true-reflection algorithm strongly indicate that a better differentiation of different tissue types may be obtained in OCT images of real tissue by using the true-reflection algorithm. This is expected to result in an improved diagnosis.

17.5 Applications of Modeling in OCT

Extraction of optical scattering parameters from OCT images is a method to obtain more quantitative information from these images in order to improve the diagnostics, that is, an alternative method of functional imaging. Accordingly, one may envisage a novel functional imaging method where, in addition to tissue morphology, parameters such as the scattering parameters, g and/or μ_s, or mean refractive index are obtained. In the following, the viability of the suggested approach in OCT is briefly discussed.

17.5.1 Extraction of Optical Scattering Properties from Tissues

As mentioned above, attenuation compensation is widely accepted within ultrasound [66]. Therefore, it has also been among the first attempts to improve on OCT imagery. In fact, attenuation compensation is a method to remove the attenuation caused by scattering in OCT images. This should improve the diagnostic capabilities due to a better differentiation of different tissue types. Until now, there have been few attempts to do attenuation compensation in OCT images of tissue by using the single-scattering OCT model [71]. However, due to the fact that multiple-scattered photons contribute to the OCT signal, the single-scattering OCT model is insufficient for this purpose. Attenuation compensation was verified on a single-layer phantom by using an OCT model taking multiple-scattering effects into account [67].

The optical scattering properties themselves, however, also contain information about the tissue. For example, cell mitochondria is affected or changed in several malignant conditions, and through these changes, the scattering changes. Conversely, provided that information about the scattering properties can be obtained with good accuracy and good (high) spatial resolution, new diagnostics can be performed. This fact is one important motivation for attempting to extract optical scattering properties in order to improve the diagnostic potential of OCT.

By using the single-scattering OCT model [2], studies have been carried out with the aim to extract only the scattering coefficient μ_s from OCT images of tissue. This approach was applied in various important applications. For example, glucose monitoring was investigated by using the single-scatter approach [72] and more recently expanded to include phase-sensitive OCT [73]. Although these investigations are of high clinical importance, more work is still needed in this area.

Determining optical scattering properties of blood is also of high importance. Faber et al. [74, 75] demonstrated that the optical absorption spectra of oxygenated and

deoxygenated hemoglobin, corrected for optical scattering, may be obtained by using spectral OCT. The underlying OCT modeling was based on a single-scattering approach. Subsequent investigations, however, have led to the conclusion that improved modeling needs to be developed in order to satisfactorily include multiple-scattering effects [76]. Single-scattering-based modeling might be applicable as demonstrated by Kodach et al. [77] showing that anisotropy and scattering parameters can be obtained from non-absorbing samples. It should be emphasized that the values for the anisotropy (approximately 0.35) is much different from those of biological tissues (approximately $>$0.85). Accordingly the results might not be transferred to biological tissues.

An important contribution by the group of van Leeuwen has been made in in vitro characterization of atherosclerotic plaque [78]. Although the model applied was based on a single-scattering model, their findings provide important data on the optical scattering coefficient of these plaques, which may influence OCT-based diagnostics in this area.

Provided an OCT model is used that takes into account multiple scattering, both μ_s and the anisotropy factor g may be extracted. Extraction for a two-layer geometry has been carried out [70, 79], where both μ_s and g were obtained for each (tissue) layer. In Ref. [70], MC simulations were used as numerical phantom as discussed in detail in the previous subsection.

A number of in vitro studies have been reported. Characterization of atherosclerotic plaque using a single, multiple-scattering layer model has been reported [80]. The method of extracting the optical scattering properties was verified using well-controlled and calibrated, single-layer tissue-like phantoms. The study provided the optical scattering properties in the 1,300-nm range for lesions in different stages including the anisotropy parameter. Based on the extracted parameters, normal tissue could be separated from malignant tissue. It should be noted that some discrepancies occur between the reported values for the scattering coefficients in Refs. [80] and [78]. Possible explanations for the differences may be due to different sample handling and fit to different models. The results reported in both Refs. [80] and [78] are encouraging, although further studies are required to fully establish these criteria and thereby demonstrate the feasibility of the method in this particular area.

In Ref. [11], an excellent study presented a rigorous application of the RTE modeling (small-angle approximation) in the extraction of optical parameters. First, the authors verified their modeling on a well-controlled tissue-like phantom. By estimating covariance and confidence regions for the extracted optical properties, they point to specific regimes of the OCT signal decay where extraction is likely to fail. These regimes depend on both the optical properties and sample beam geometry. Hence, their findings provide important insight of how to optimize the OCT system for a specific application. The authors applied their method to cervical tissue (cervical dysplasia 2–3 and leukoplakia). In their in vitro investigation, they demonstrated that cervical dysplasia 2–3 and leukoplakia could be distinguished on the basis of the extracted optical scattering properties. Hence, their excellent contribution should be an encouragement for expanding to other clinical applications and finally in vivo applications.

Related to this work, Samatham et al. [81] develop a method for extracting optical properties of skin samples (from a mouse) based on reflectance-mode

confocal laser scanning microscopy. Their approach might be relevant for optical coherence microscopy and even find applications in OCT extraction of optical properties in vivo.

In vivo studies are sparse; however, Knüttel et al. [82] took the approach of extracting optical scattering properties and refractive index aiming at relating the effects of skin hydration to the optical properties extracted from OCT images. Their investigation showed the applicability of the approach and the potential in dermatology to provide new diagnostic information.

17.6 Wigner Phase-Space Distribution Function for the OCT Geometry

Recently, the Wigner phase-space distribution [83] for multiple light scattering in biological media has received considerable attention. This is because it has been suggested by numerous authors that new venues for medical imaging may be based on coherence tomography using measurements of Wigner phase-space distributions [23, 24, 84–86]. It has been suggested that the Wigner phase-space distribution is particularly useful for biomedical imaging because the phase-space approach provides maximum information, that is, both space and momentum (angular) information, about the light being used. This section is devoted to the derivation of a closed-form solution for the Wigner phase-space distribution function [23] obtained directly from the EHF [37] solution for the optical field.

In all cases considered in this section, as well as in Refs. [24, 84–86], the Wigner phase-space distribution function is positive definite, and hence, the Wigner function and the specific radiance may be used interchangeably. We are primarily concerned with a standard OCT propagation geometry shown in Fig. 17.1, and as such, we consider a sample beam reflected at a discontinuity giving rise to diffuse backscattering. This section deals with the reflection geometry only; for the transmission geometry, the reader is referred to Refs. [23, 85].

17.6.1 General Considerations

Consider a cw quasi-monochromatic optical wave propagating through a non-absorbing random small-angle scattering medium, reflecting off a discontinuity giving a diffuse reflection, and subsequently propagating back to the initial plane. Denote the resulting optical field in the initial plane, perpendicular to the optic axis, by $U(\mathbf{P})$, where $\mathbf{P}$ is a two-dimensional vector in this plane. For simplicity in notation, we omit the time dependence. The Wigner phase-space distribution, $W(\mathbf{P},\mathbf{q})$, may be written as [87]

$$W(\mathbf{P},\mathbf{q}) = \int \frac{d\mathbf{p}}{(2\pi)^2} \langle U(\mathbf{P}+\mathbf{p}/2)U^*(\mathbf{P}-\mathbf{p}/2)\rangle \exp[i\mathbf{q}\cdot\mathbf{p}], \tag{17.65}$$

where angular brackets denote the ensemble average. That is, the Wigner phase-space distribution function is a two-dimensional Fourier transform of the indicated mutual coherence function $\langle U(\mathbf{P}+\mathbf{p}/2)U^*(\mathbf{P}-\mathbf{p}/2)\rangle$ and, as such, contains the same information about the optical field as does the mutual coherence function. The quantity $\mathbf{q}$ is a transverse momentum, and in the small-angle approximation, its magnitude q can be related directly to the scattering angle simply as $q = 2k\sin\theta/2 \approx k\theta$, where is the free-space wave number. In addition, because in the small-angle approximation the differential element of solid angle $d\Omega = 2\pi\sin\theta \mathrm{d}\theta \approx 2\pi\theta \mathrm{d}\theta = 2\pi q \mathrm{d}q/k^2$, it is easily verified that the integral of $W(\mathbf{P},\mathbf{q})$ over all $\mathbf{q}$ (i.e., over solid angle) equals the intensity $I(\mathbf{P})$, that is, $|U(\mathbf{P})|^2$, at the observation point $\mathbf{P}$. Hence, to within a multiplicative constant, the Wigner phase-space distribution is equal to the specific radiance distribution of the optical field at the observation point of interest for those cases where the Wigner phase-space distribution is positive definite. To be specific, the specific radiance distribution $N(\mathbf{P},\theta) = k^2 W(\mathbf{P},k\theta)$ in those cases.

Here, we neglect polarization effects, bulk backscattering, and enhanced backscattering, which is obtained very close to the optical axis. In random media where the scattering particles are large compared to the wavelength and the index of refraction ratio is near unity, the bulk backscatter efficiency is much smaller than the scattering efficiency. Moreover, the scattering is primarily in the forward direction, which is the basis of using the paraxial approximation. Therefore, the bulk backscattering may be neglected when considering the light propagation problem, since its contribution is small. An example of this is skin tissue (cell sizes of 5–10-μm diameter and index of refraction ratio of 1.45/1.4 = 1.04).

It is well known that a medium with random scattering inhomogeneities will produce an amplification effect of the mean intensity in the strictly backward direction, as compared to the corresponding intensity obtained in the homogeneous medium [88]. This so-called enhanced backscattering is due to multichannel coherence effects (i.e., interference at a source point between waves transmitted in the forward and backward directions by the same inhomogeneities in the medium). Additionally, because of conservation of energy, enhanced backscattering is accompanied by a corresponding reduction in intensity in directions close to the strictly backward direction. In general, as discussed in Ref. [88], the linear dimension of the region surrounding the strictly backward direction where enhanced backscattering is obtained is of the order or less than the transverse intensity correlation length, l. The corresponding reduction of intensity occurs near the surface of a cone of angle of the order l/Z, where Z is the (one way) propagation distance in the medium. Strictly speaking, enhanced backscattering effects are obtained in situations where the linear dimensions of the illuminated region, a, in the backscattering plane satisfy $a^2 << \lambda Z$, where λ is the wavelength. When the radiation at some point $\mathbf{P}$ in the observation plane results from illuminated regions that are large compared to $[\lambda Z]^{1/2}$, $\mathbf{P}$ will not be in the strictly backscattered direction with respect to the reflected light and, as a consequence, enhanced backscattering will not be manifested. In all cases considered here, $a >> [\lambda Z]^{1/2}$ and, therefore, enhanced backscattering effects are neglected.

As indicated in Fig. 17.1, the signal of interest results from diffuse reflection at the discontinuity of interest only. As discussed above, the statistics of the forward and back propagating optical waves are assumed here to be independent. This case has been treated in Sect. 17.2, and from (17.21) with $\mathbf{p}_{1,2} = \mathbf{P} \pm \mathbf{p}/2$, the EHF solution for the mutual coherence function for diffuse reflection in the discontinuity plane, and observation in the lens plane, is given by

$$\langle U(\mathbf{P}+\mathbf{p}/2)U^*(\mathbf{P}-\mathbf{p}/2)\rangle = \frac{4\pi}{k^2}\int d\mathbf{r}\langle I_B(\mathbf{r})\rangle G_0(\mathbf{r},\mathbf{P}+\mathbf{p}/2)G_0^*(\mathbf{r},\mathbf{P}-\mathbf{p}/2)\Gamma_{pt}(\rho). \tag{17.66}$$

$\langle I_B(r)\rangle$ is the mean backscattered irradiance distribution in the plane of the discontinuity, $\Gamma_{pt}(p)$ is the mutual coherence function of a point source located in the discontinuity plane and observed in the lens plane, where $p = |\mathbf{p}_1 - \mathbf{p}_2|$, and $G_0(\mathbf{r},\mathbf{p})$ is the Huygens-Fresnel Green's function for homogeneous media given, in general, by [40]

$$G_0(\mathbf{r},\mathbf{p}) = -\frac{ik}{2\pi B_b}\exp\left[-\frac{ik}{2B_b}\left(A_b r^2 - 2\mathbf{r}\cdot\mathbf{p} + D_b p^2\right)\right], \tag{17.67}$$

where A_b, B_b, and D_b are the (real) ABCD ray-matrix elements for backpropagation through the optical system (because we are dealing with "real" ABCD optical systems, we tacitly assume that $B \neq 0$). To be as general as possible, we assume an arbitrary ABCD optical system between the lens and discontinuity planes, respectively. For the OCT geometry, we have $A_b = D_b = 1$ and $B_b = d + z/n$, where d is the distance from the lens to the tissue surface, n is the mean index of refraction of the tissue, and z is the depth of the discontinuity. In (17.66), the positive definite quantity Γ_{pt} is the mutual coherence of a point source located in the discontinuity plane and observed in the initial lens plane, that is, the mutual coherence function for backward propagation through the medium. This quantity is given by [45]

$$\Gamma_{pt}(p) = \exp\{-s[1 - b_\phi(p)]\}, \tag{17.68}$$

where the optical depth $s = \mu_s z$. The quantity μ_s is the bulk scattering coefficient, and $b_\phi(p)$ is the normalized phase autocorrelation function of a point source whose origin is in the discontinuity plane given by [45]

$$b_\phi(p) = \frac{\int_0^z dz' \int_0^\infty \sigma(\theta;z')J_0(kp_s\theta)\theta d\theta}{\int_0^z dz' \int_0^\infty \sigma(\theta;z')\theta d\theta}, \tag{17.69}$$

J_0 is the Bessel function of the first kind of order zero,

$$p_s = \frac{B_b(z')}{B_b}p, \tag{17.70}$$

where $B_b(z')$ is the B-matrix element for backpropagation from the discontinuity plane to a distance z' and $\sigma(\theta;z')$ is interpreted as the volume scattering function as a function of position measured from the discontinuity plane in the optical system [40]. Strictly speaking, (17.68) applies to the case where the scattering is in the near-forward direction and all of the scattered light being contained within the collection solid angle of the optical system being used. For propagation in an inhomogeneous medium where appreciable light is scattered outside of the collection solid angle, the mutual coherence function of (17.68) becomes $\Gamma_{pt}(p) = \exp\{-s_W - s_N[1 - b_\phi(p)]\}$, where the subscripts N and W refer to the near-forward and wide-angle contributions to the optical depth, respectively [23, 24, 86]. That is, the portion of the light scattered outside of the collection solid angle thus appears much like an effective absorption coefficient for propagation in the near-forward direction. We note that all correlation functions of interest here can be expressed directly in terms of the spectral densities via the relation $\sigma(\theta) = 2\pi k^4 \Phi_n(k\theta)$, where Φ_n is the three-dimensional spectrum of the index of refraction inhomogeneities, and we have omitted the functional dependence on path length for notational simplicity [52]. For the OCT geometry, we have $\sigma(\theta;z') = \sigma(\theta)$ for $0 \le z' \le z$, and 0 otherwise; $B_b(z') = z'/n$ for $0 \le z' \le z$ and $B_b(\mathrm{z}') = \mathrm{z}/n + z' - z$ for $z \le z' \le d + z$.

In this section, it is tacitly assumed that we are dealing with a statistically stationary and isotropic random medium. Then, it is well known that all second-order spatial correlation functions of the optical field, such as $\Gamma_{pt}(p)$, are functions of the magnitude of the difference of the spatial coordinates and satisfy the identity $\Gamma_{pt}(-p) = \Gamma_{pt}^{*}(p)$ [52].

Because the point source mutual coherence function given in (17.68) is valid for arbitrary values of the optical depth s [52], the results given below for the Wigner phase-space distribution function are valid in both the single- and multiple-scattering regimes, that is, arbitrary values of s.

Substituting (17.66) and (17.67) into (17.65) and simplifying yield

$$W(\mathbf{P},\mathbf{q}) = \frac{1}{\pi B^2}\int \frac{d\mathbf{p}}{(2\pi)^2}\exp\left[i\mathbf{p}\cdot\left(\mathbf{q} - \frac{kD}{B}\mathbf{P}\right)\right]\Gamma_{pt}(p)H(\mathbf{p}), \tag{17.71}$$

where

$$H(\mathbf{p}) = \int d\mathbf{r}\langle I_B(\mathbf{r})\rangle \exp\left[i\frac{k}{B_b}\mathbf{p}\cdot\mathbf{r}\right] \tag{17.72}$$

is related to the Fourier transform of $\langle I_B(\mathbf{r})\rangle$. In Ref. [23], it is shown that

$$H(\mathbf{p}) = R_d\Gamma_{pt}(-p)K(-\mathbf{p}) = R_d\Gamma_{pt}^{*}(p)K(-\mathbf{p}), \tag{17.73}$$

where R_d is the reflection coefficient of the discontinuity,

$$K(\mathbf{r}) = \int d\mathbf{R}U_{Si}(\mathbf{R} + \mathbf{r}/2)U_{Si}^{*}(\mathbf{R} - \mathbf{r}/2)\exp\left[-i\frac{kA}{B}\mathbf{r}\cdot\mathbf{R}\right], \tag{17.74}$$

and $U_{Si}(\mathbf{r})$ is the initial optical wave function. Substituting (17.73) into (17.71) yields

$$W(\mathbf{P},\mathbf{q}) = \frac{R_d}{\pi B_b^2}\int \frac{d\mathbf{p}}{(2\pi)^2}\left|\Gamma_{pt}(p)\right|^2 K(-\mathbf{p})\exp\left[i\mathbf{p}\cdot\left(\mathbf{q}-\frac{kD_b}{B_b}\mathbf{P}\right)\right]$$
$$= \frac{R_d}{2\pi^2 B_b^2}\int_0^\infty dpp\left|\Gamma_{pt}(p)\right|^2 K(p)J_0\left(\left|\mathbf{q}-\frac{kD_b}{B_b}\mathbf{P}\right|p\right) \quad (17.75)$$
(for axially symmetric U_{Si}).

This is the required general solution for the Wigner phase-space distribution function for diffuse reflection in the paraxial approximation. That is, for a given initial optical wave function and a medium whose scattering function is known, (17.75) is the solution for the Wigner phase-space distribution function, that is, specific radiance. Note that $I(\mathbf{P}) = \int W(\mathbf{P},\mathbf{q})d\mathbf{q} = R_d P_0/\pi B_b{}^2$, where P_0 is the transmitted power. As expected for diffuse reflection, the intensity in the observation plane is constant, independent of position.

17.6.1.1 Comments

For general scattering functions $\sigma(\theta)$, the integral indicated in (17.75) cannot be obtained analytically, although numerical results can be readily obtained. However, some general features of the Wigner phase-space distribution function can be obtained by direct examination of the general formula. First, examination of (17.75) reveals that, in general, the Wigner phase-space distribution attains its maximum along the line given by $\mathbf{P} = B_b\mathbf{q}/kD_b = B_b\boldsymbol{\theta}/D_b$. Additionally, because $\Gamma_{pt}(p)$ in (17.68) can be rewritten as

$$\Gamma_{pt}(p) = e^{-s} + e^{-s}\left(\exp\left[sb_\phi(p)\right] - 1\right), \quad (17.76)$$

we can conclude, from (17.75) and (17.76), that, in general, the Wigner phase-space distribution function consists of three terms. The square of the first term on the right-hand side of (17.76), which corresponds to the ballistic photons, leads to an attenuated distribution of what would be obtained in the absence of the scattering inhomogeneities. The square of the corresponding second term represents a broader halo resulting from multiple scattering in the medium. The third term is a cross term between the ballistic and multiple-scattering contributions, respectively. Physically, the cross term is the coherent mixing of the unscattered and multiple-scattered light.

Next, for sufficiently large values of the optical depth s, examination of (17.68) reveals that Γ_{pt} is nonzero for $s[1 - b_\phi(p)]$ less than the order unity, that is, for $b_\phi(p)$ near unity. Expanding $b_\phi(p)$ in powers of p and retaining the first two nonzero terms allows one to obtain asymptotic results. In the limit $s >> 1$, for all cases of practical concern, the resulting width of $|\Gamma_{pt}(p)|^2$ is much narrower than $K(p)$, and without loss of generality, we may replace $K(p)$ by its value at the origin $K(0) = P_0$, the transmitted power (see (17.74)).

17.6.2 Applications to Optical Coherence Tomography

It follows from the analysis in Sect. 17.2 that the signal-to-noise ratio (*SNR*) in a standard OCT system can be expressed as

$$SNR = \text{constant} \times \text{Re}\left[\iint \Gamma_R(\mathbf{P}+\mathbf{p}/2, \mathbf{P}-\mathbf{p}/2)\Gamma_S(\mathbf{P}+\mathbf{p}/2, \mathbf{P}-\mathbf{p}/2)d\mathbf{P}d\mathbf{p}\right], \tag{17.77}$$

where denotes the real part and Γ_R and Γ_S are the mutual coherence functions of the (deterministic) reference beam and sample beam in the mixing plane, respectively. Because the Wigner phase-space distribution function and the mutual coherence function are Fourier transform related (see (17.65)), the *SNR* can be rewritten as

$$SNR = \text{constant} \times \text{Re}\left[\iint W_R(\mathbf{P}, -\mathbf{q})W_S(\mathbf{P}, \mathbf{q})d\mathbf{P}d\mathbf{q}\right], \tag{17.78}$$

where W_R and W_S are the corresponding Wigner phase-space distribution functions of the reference and sample beams, respectively. Equation (17.78) indicates, in particular, that the *SNR* of a standard OCT system is related globally to the Wigner phase-space distribution function of the sample beam. That is, images obtained from standard OCT systems contain global, rather than local, information of the Wigner phase-space distribution function of the sample beam. Improved OCT imagery can thus only be obtained from systems that make use of the local properties of the Wigner phase-space distribution function, rather than globally where information is inevitably lost. Below, we derive expressions for the Wigner phase-space distribution function of the sample beam for a standard OCT geometry for both classes of scattering functions discussed in Ref. [23].

Consider an OCT system where the initial optical wave function (i.e., immediately following the lens) is given by

$$U_{Si}(r) = \sqrt{\frac{P_0}{\pi w_0^2}}\exp\left[-\frac{r^2}{2}\left(\frac{1}{w_0^2}+\frac{ik}{f}\right)\right]. \tag{17.79}$$

For an OCT system, focusing at a tissue discontinuity at depth z, we then get the following equation for $K(r)$

$$K(r) = P_0 \exp\left[-\frac{r^2}{4w_0^2}\right], \tag{17.80}$$

and using (17.78), the heterodyne efficiency factor for the OCT signal for such a system may be written as

$$\Psi \equiv \frac{SNR}{SNR_0} = \frac{\int |K(\mathbf{p})|^2 \left|\Gamma_{pt}(\mathbf{p})\right|^2 d\mathbf{p}}{\int |K(\mathbf{p})|^2 d\mathbf{p}}. \tag{17.81}$$

We now obtain analytic engineering approximations for the Wigner phase-space distribution function, valid for all values of s, for b_ϕ that are quadratic near the origin. Substituting (17.17) in Ref. [23] and (17.80) into (17.75) and simplifying yield

$$W(\mathbf{P},\mathbf{q}) \cong \frac{R_d P_0 4w_0^2}{(2\pi f)^2}\left[e^{-2s}\exp\left(-Q^2w_0^2\right) + e^{-s}(1-e^{-s})\frac{\tilde{\rho}_0^2}{4w_0^2}\exp\left(-\frac{Q^2\tilde{\rho}_0^2}{4}\right) + (1-e^{-s})^2\frac{\tilde{\rho}_0^2}{8w_0^2}\exp\left(-\frac{Q^2\tilde{\rho}_0^2}{8}\right)\right], \tag{17.82}$$

where

$$\frac{1}{\tilde{\rho}_0^2} = \frac{1}{\rho_0^2} + \frac{1}{4w_0^2}, \tag{17.83}$$

$$\rho_0 = \sqrt{\frac{3}{s}}\frac{\lambda}{\pi\theta_{rms}}\left(\frac{nf}{z}\right). \tag{17.84}$$

Here, $Q = |\mathbf{q} - (k/f)\mathbf{P}|$. The first, second, and third terms on the right-hand side of (17.82) represent the ballistic, cross, and multiple-scattering contributions to the Wigner phase-space distribution function discussed below (17.76), respectively.

In the limit of $s << 1$, examination of (17.82) reveals that for $\mathbf{P} = \mathbf{0}$, the $1/e$ transverse momentum width, Δ_q, of the Wigner phase-space distribution is given by $\Delta_q = 1/w_0$. Furthermore, in the limit $s >> 1$, $\Delta_q = 2\sqrt{2}\tilde{\rho}_0^{-1}$, where $\tilde{\rho}_0 \cong \rho_0$. In this case, $\Delta_q \propto z^{3/2}$ in the presence of the shower-curtain effect, which manifests itself in the standard OCT geometry. For comparison, $\Delta_q \propto z^{1/2}$ in the absence of the shower-curtain effect.

We have not been able to obtain a corresponding analytic approximation, valid for all values of s, for the Henyey-Greenstein type of scattering function [23]. For this case, we can only conclude that

$$W(\mathbf{P},\mathbf{q}) \cong \frac{R_d P_0}{(2\pi f)^2}(1-2s)\exp\left[-Q^2w_0^2\right], \quad s << 1, \tag{17.85}$$

and

$$W(\mathbf{P},\mathbf{q}) \cong \frac{R_d P_0}{\pi(2\pi f)^2}\left(\frac{r_0}{s}\right)^2 \frac{1}{\left(1+\left(\frac{r_0}{s}\right)^2\left|\mathbf{q}-\frac{k}{f}\mathbf{P}\right|^2\right)^{3/2}}, \quad s >> 1, \tag{17.86}$$

where $r_0 = \{[\lambda g^{1/2}]/[2\pi(1-g)]\}[nf/z]$. In the limit of $s << 1$, examination of (17.85) reveals that for $\mathbf{P} = \mathbf{0}$, the $1/e$ transverse momentum width, Δ_q,

of the Wigner phase-space distribution is given by $\Delta_q = 1/w_0$. Furthermore, in the limit $s >> 1$, it is obtained from (17.86) that $\Delta_q = s/r_0$. In this case, $\Delta_q \propto z^2$ in the presence of the shower-curtain effect. For comparison, $\Delta_q \propto z$ in the absence of the shower-curtain effect.

It is important to note that for both types of scattering functions, the momentum width increases with increasing depth as z^{γ}, with considerably larger values of γ being obtained in the presence of the shower-curtain effect. Furthermore, the actual value of γ is highly dependent on the details of the scattering function [23].

As shown above, it is possible to determine the lateral coherence length of the sample field from measurements of the Wigner phase-space distribution. As is evident from (17.84), the lateral coherence length depends on the optical parameters of the tissue, that is, n, μ_s, and θ_{rms}. Therefore, it is feasible to create images based on measurements of the lateral coherence length as a function of position in the tissue. In contrast to OCT signals used to create conventional OCT images, the lateral coherence length is related only to the propagation of the light in the tissue, and its magnitude is independent of the amount of light backscattered or reflected at the probed depth.

In general, a discontinuity between two tissue layers is characterized by a change of the scattering coefficient, the backscattering coefficient, and the index of refraction. The relative change of the scattering coefficient and the backscattering coefficient is markedly greater than the corresponding relative change in the index of refraction [43]. In human skin tissue, for example, the scattering coefficients of epidermis and dermis are 50 and 21.7 mm^{-1}, respectively, while the indices of refraction are lying in the range 1.37–1.5 [43]. On this basis, it can be shown from the analysis above that an imaging system, based on measurements of the lateral coherence length, may have a higher sensitivity to changes in the scattering coefficient than the conventional OCT system probing the corresponding change in the backscattering coefficient. The higher sensitivity may lead to an improved contrast in the obtained image. This model and the above discussion give more insight into the ideas presented recently that new venues for medical imaging may be based on coherence tomography using measurements of Wigner phase-space distributions [23, 24, 84–86].

17.7 Appendix A

The 4F system described in Sect. 17.3.1 is inspected where we have designated three transverse coordinate planes (see Fig. 17.6): the p-plane coinciding with the optical fiber, the q-plane coinciding with the diffusely reflecting discontinuity within the sample, and the r-plane coinciding with the right side of the thin focusing lens at $z = -d$. By applying approximations identical to those used in Ref. [10], we now wish to show the following two statements. Firstly, that the heterodyne efficiency factor, defined by the cross correlations of the sample

and reference fields at the p-plane, may be written in terms of their respective intensities only, so that

$$\Psi_p = \frac{\langle i^2 \rangle}{\langle i_0^2 \rangle} = \frac{\int I_R(\mathbf{p}) \langle I_s(\mathbf{p}) \rangle d^2\mathbf{p}}{\int I_R(\mathbf{p}) \langle I_{s0}(\mathbf{p}) \rangle d^2\mathbf{p}}, \tag{17.A1}$$

where the integrals are taken over the p-plane and I_R, $\langle I_S(\mathbf{p}) \rangle$, and $\langle I_{S0}(\mathbf{p}) \rangle$ are the intensities of the reference, the ensemble average of the reflected light from the discontinuity, and the ensemble average of the reflected light from the discontinuity in the absence of scattering, respectively. Secondly, that this calculation of the heterodyne efficiency factor Ψ in the p-plane, Ψ_p, is mathematically identical to calculating Ψ in the r-plane, Ψ_r, as given by (17.57), so that

$$\begin{aligned} \Psi_r &= \frac{\mathrm{Re}\left[\iint \Gamma_R(\mathbf{r}_1, \mathbf{r}_2) \langle \Gamma_S(\mathbf{r}_1, \mathbf{r}_2) \rangle d\mathbf{r}_1 d\mathbf{r}_2\right]}{\mathrm{Re}\left[\iint \Gamma_R(\mathbf{r}_1, \mathbf{r}_2) \langle \Gamma_{S0}(\mathbf{r}_1, \mathbf{r}_2) \rangle d\mathbf{r}_1 d\mathbf{r}_2\right]} \\ &= \frac{\mathrm{Re}\left[\iint \Gamma_R(\mathbf{p}_1, \mathbf{p}_2) \langle \Gamma_S(\mathbf{p}_1, \mathbf{p}_2) \rangle d\mathbf{p}_1 d\mathbf{p}_2\right]}{\mathrm{Re}\left[\iint \Gamma_R(\mathbf{p}_1, \mathbf{p}_2) \langle \Gamma_{S0}(\mathbf{p}_1, \mathbf{p}_2) \rangle d\mathbf{p}_1 d\mathbf{p}_2\right]} = \Psi_p. \end{aligned} \tag{17.A2}$$

To outline the derivation, the proof will be initiated by finding the field U_S due to an initial field propagating from the r-plane toward the sample and reflecting off the discontinuity. This field is then used to calculate the cross correlation $\langle \Gamma_S(\mathbf{p}_1, \mathbf{p}_2) \rangle = \langle U_S(\mathbf{p}_1) U_S^*(\mathbf{p}_2) \rangle$, and it is shown that U_S is delta-correlated [19] and thus the validity of (17.A1) is demonstrated. It is then demonstrated that the obtained expression for Ψ_p is identical to (17.81). Because we are only concerned with the ratio Ψ, any multiplicative constant not related to the properties of the scattering medium is omitted.

Using the Huygens-Fresnel principle, the field at the p-plane, U_S, due to a field immediately to the right of the focusing lens in the r-plane, U_r, is given by

$$U_s(\mathbf{r}, \mathbf{p}) = \int U_r(\mathbf{r}) G_{r-p}(\mathbf{r}, \mathbf{p}) d^2\mathbf{r}, \tag{17.A3}$$

where $G_{r\text{-}p}(\mathbf{r},\mathbf{p})$ is the Huygens-Fresnel Green's function for propagation from the r-plane to the p-plane. For a general ABCD matrix system, this Green's function is given by [40]

$$G_0(\mathbf{r}, \mathbf{p}) = -\frac{ik}{2\pi B} \exp\left[-\frac{ik}{2B}\left(Ar^2 - 2\mathbf{r} \cdot \mathbf{p} + Dp^2\right)\right], \tag{17.A4}$$

where A, B, and D are the matrix elements and the notation r denotes the length of the vector $\mathbf{r}$. For the propagation from r to p, $A = -1$, $B = f$, and $D = -1$. The field

at the r-plane due to a field, U_q, impinging upon the discontinuity is found using the EHF principle

$$U_r(\mathbf{r}) = \int \eta(\mathbf{q}) U_q(\mathbf{q}) G_f(\mathbf{q}, \mathbf{r}) \exp[i\varphi(\mathbf{q}, \mathbf{r})] d^2\mathbf{q}, \tag{17.A5}$$

where G_f is the Green's function for propagating the optical distance f given by (17.A4) with the matrix elements $A = 1$, $B = f$, and $D = 1$. $\varphi(\mathbf{q},\mathbf{r})$ is the stochastic phase added to the phase of a spherical wave propagating from $\mathbf{q}$ to $\mathbf{r}$ due to the scattering medium, and $\eta(\mathbf{q})$ is a complex reflection coefficient due to the discontinuity. Calculating the cross correlation of the field U_S yields

$$\begin{aligned} \Gamma_s(\mathbf{p}_1, \mathbf{p}_2) = \iiiint & G_f(\mathbf{q}, \mathbf{r}) G_f^*(\mathbf{q}', \mathbf{r}') G_{r-p}(\mathbf{r}, \mathbf{p}_1) G_{r-p}^*(\mathbf{r}', \mathbf{p}_2) \\ & \times \langle U_q(\mathbf{q}) U_q^*(\mathbf{q}') \rangle \langle \eta(\mathbf{q}) \eta(\mathbf{q}') \rangle \\ & \times \langle \exp[i\varphi(\mathbf{q}, \mathbf{r}) - i\varphi(\mathbf{q}', \mathbf{r}')] \rangle d^2\mathbf{r} d^2\mathbf{r}' d^2\mathbf{q} d^2\mathbf{q}', \end{aligned} \tag{17.A6}$$

where primed variables are related to $U_S{}^*$, and we have assumed that the scattering medium and the properties of the diffusely discontinuity are independent. It should also be noted that in writing $\langle U_q(\mathbf{q}) U_q{}^*(\mathbf{q}') \exp[i\varphi(\mathbf{q}, \mathbf{r}) - i\varphi(\mathbf{q}', \mathbf{r}')] \rangle = \langle U_q(\mathbf{q}) U_q{}^*(\mathbf{q}') \rangle \times \langle \exp[i\varphi(\mathbf{q}, \mathbf{r}) - i\varphi(\mathbf{q}', \mathbf{r}')] \rangle$, it has been assumed that the phase distortion due to the scattering medium added to the field propagating from L2 to the discontinuity is statistically independent of that added to the field propagating from the discontinuity to L2. The validity of this assumption in MC simulations is discussed in Sect. 17.3.3. Because the discontinuity is diffusely reflecting $\langle \eta(\mathbf{q}) \eta(\mathbf{q}') \rangle = (4\pi/k^2) \delta(\mathbf{q} - \mathbf{q}')$, where $\delta(\mathrm{r})$ is the two-dimensional Dirac's delta function [39]. This yields

$$\begin{aligned} \Gamma_s(\mathbf{p}_1, \mathbf{p}_2) = \iiint & G_f(\mathbf{q}, \mathbf{r}) G_f^*(\mathbf{q}, \mathbf{r}') G_{r-p}(\mathbf{r}, \mathbf{p}_1) G_{r-p}^*(\mathbf{r}', \mathbf{p}_2) \\ & \times \langle I_q(\mathbf{q}) \rangle \Gamma_{PT}(\mathbf{r} - \mathbf{r}') d^2\mathbf{r} d^2\mathbf{r}' d^2\mathbf{q}, \end{aligned} \tag{17.A7}$$

where Γ_{PT} is given by (17.41) and I_q is the intensity of the field U_q. The average intensity $\langle I_q(\mathbf{q}) \rangle$ can be found from (17.39), and it is noted that the difference vector, $\boldsymbol{\rho}$, in (17.39) is independent of $\mathbf{r}$ and $\mathbf{r}'$ in (17.A7). Now, invoking the sum and difference coordinates $\mathbf{R} = \frac{1}{2}(\mathbf{r} + \mathbf{r}')$ and $\boldsymbol{\rho} = \mathbf{r} - \mathbf{r}'$ and performing the q-integration and the ρ-integration originating from (17.39) yield

$$\begin{aligned} \Gamma_s(\mathbf{p}_2, \mathbf{p}_2) = \iint & \exp\left[-\frac{ik}{2f} \{ p_2^2 - p_1^2 - \boldsymbol{\rho} \cdot (\mathbf{p}_1 + \mathbf{p}_2) + 2\mathbf{R} \cdot (\mathbf{p} - \mathbf{p}_1) \} \right] \\ & \times |\Gamma_{PT}(\boldsymbol{\rho})|^2 K(-\boldsymbol{\rho}) d^2\boldsymbol{\rho} d^2\mathbf{R}, \end{aligned} \tag{17.A8}$$

where we have used the relation

$$\int \exp[i\mathbf{m}\cdot(\mathbf{u}+\mathbf{v})]d^2\mathbf{m} = (2\pi)^2\delta(\mathbf{u}+\mathbf{v}). \tag{17.A9}$$

Carrying out the **R**-integration then yields

$$\begin{aligned}\Gamma_s(\mathbf{p}_2,\mathbf{p}_2) =& \delta(\mathbf{p}_2-\mathbf{p}_1)\int \exp\left[-\frac{ik}{2f}\{p_2^2-p_1^2-\boldsymbol{\rho}\cdot(\mathbf{p}_1+\mathbf{p}_2)\}\right] \\ &\times |\Gamma_{PT}(\boldsymbol{\rho})|^2 K(-\boldsymbol{\rho})d^2\boldsymbol{\rho}\end{aligned} \tag{17.A10}$$

which shows the sample U_S to be delta-correlated, and thus, (17.A1) is proven.

To calculate (17.A1), we consider (17.A8) for the case $\mathbf{p}_1 = \mathbf{p}_2 = \mathbf{p}$, which then yields the intensity

$$\langle I_s(\mathbf{p})\rangle = A_{lens}\int \exp\left[-\frac{ik}{f}\boldsymbol{\rho}\cdot\mathbf{p}\right]|\Gamma_{PT}(\boldsymbol{\rho})|^2 K(-\boldsymbol{\rho})d^2\boldsymbol{\rho}, \tag{17.A11}$$

where A_{lens} is the area of the focusing lens.

To find the OCT signal $\langle i^2\rangle$, we now insert (17.A11) into the numerator of (17.A1)

$$\begin{aligned}\langle i^2\rangle &= \iint \exp\left[-\frac{ik}{2f}(-2\boldsymbol{\rho}\cdot\mathbf{p})\right]|\Gamma_{PT}(\boldsymbol{\rho})|^2 K(-\boldsymbol{\rho})I_R(\mathbf{p})d^2\boldsymbol{\rho}d^2\mathbf{p} \\ &= \int |\Gamma_{PT}(\boldsymbol{\rho})|^2|K(\boldsymbol{\rho})|^2 d^2\boldsymbol{\rho},\end{aligned} \tag{17.A12}$$

where we have used that the reference field impinging on the reference mirror may be calculated using (17.39) with $\Gamma_{PT} = 1$ and $A = 1$ and $B = f$. Because the p-plane is the conjugate plane to the plane of the reference mirror, the field here is identical to that impinging upon the reference mirror. Γ_{PT} is unity in the absence of scattering, so it is now easy to see that Ψ may be calculated through

$$\Psi_p = \frac{\int |\Gamma_{PT}(\boldsymbol{\rho})|^2|K(\boldsymbol{\rho})|^2 d^2\boldsymbol{\rho}}{\int |K(\boldsymbol{\rho})|^2 d^2\boldsymbol{\rho}}. \tag{17.A13}$$

Note that the integration is over the r-plane. It is seen that Ψ_p is identical to Ψ_r given by (17.81). It has thus been proven that within the approximation of the EHF principle, the heterodyne efficiency factor of the OCT system depends solely upon the intensity distributions of the reference and sample fields in the p-plane. Furthermore, it is straightforward to prove that this will be true for any conjugate plane to a diffusely reflecting discontinuity plane within the sample.

One should note that there exists an ambiguity between obtaining a delta function in (17.A10) and obtaining a finite area of the focusing lens in (17.A11). Firstly, this area is irrelevant for the heterodyne efficiency factor, and no assumption of a finite lens area is made in Sect. 17.2.2. Furthermore, it is easy to show that (17.A13) is just as well obtained by inserting (17.A10) into (17.A2). Secondly, a finite radius of the focusing lens would have yielded an Airy function in $R_A(\mathbf{p}_1 - \mathbf{p}_2)$ instead of a delta function, where R_A is the radius of aperture. Thus, if the aperture is large, the sample field will be essentially delta-correlated in the p-plane.

References

1. D. Huang, E.A. Swanson, C.P. Lin, J.S. Schuman, W.G. Stinson, W. Chang, M.R. Hee, T. Flotte, K. Gregory, C.A. Puliafito, J.G. Fujimoto, Optical coherence tomography. Science **254**, 1178–1181 (1991)
2. J.M. Schmitt, A. Knüttel, R.F. Bonner, Measurement of optical properties of biological tissues by low-coherence reflectometry. Appl. Opt. **32**, 6032–6042 (1993)
3. J.M. Schmitt, A. Knüttel, A.S. Gandjbakhche, R.F. Bonner, Optical characterization of dense tissues using low-coherence interferometry. Proc. SPIE **1889**, 197–211 (1993)
4. M.J. Yadlowsky, J.M. Schmitt, R.F. Bonner, Multiple scattering in optical coherence microscopy. Appl. Opt. **34**, 5699–5707 (1995)
5. M.J. Yadlowsky, J.M. Schmitt, R.F. Bonner, Contrast and resolution in the optical coherence microscopy of dense biological tissue. Proc. SPIE **2387**, 193–203 (1995)
6. Y. Pan, R. Birngruber, R. Engelhardt, Contrast limits of coherence-gated imaging in scattering media. Appl. Opt. **36**, 2979–2983 (1997)
7. L.S. Dolin, A theory of optical coherence tomography. Radiophys. Quant. Electron. **41**, 850–873 (1998)
8. J.M. Schmitt, A. Knüttel, Model of optical coherence tomography of heterogeneous tissue. J. Opt. Soc. Am. A **14**, 1231–1242 (1997)
9. D.J. Smithies, T. Lindmo, Z. Chen, J.S. Nelson, T.E. Milner, Signal attenuation and localization in optical coherence tomography studied by Monte Carlo simulation. Phys. Med. Biol. **43**, 3025–3044 (1998)
10. L. Thrane, H.T. Yura, P.E. Andersen, Analysis of optical coherence tomography systems based on the extended Huygens-Fresnel principle. J. Opt. Soc. Am. A **17**, 484–490 (2000)
11. I.V. Turchin, E.A. Sergeeva, L.S. Dolin, V.A. Kamensky, N.M. Shakhova, R. Richards-Kortum, Novel algorithm of processing optical coherence tomography images for differentiation of biological tissue pathologies. J. Biomed. Opt. **10**, 064024 (2005)
12. A. Tycho, T.M. Jørgensen, H.T. Yura, P.E. Andersen, Derivation of a Monte Carlo method for modeling heterodyne detection in optical coherence tomography systems. Appl. Opt. **41**, 6676–6691 (2002)
13. H. Kahn, T.E. Harris, Estimation of particle transmission by random sampling, in *Monte Carlo Methods*. National Bureau of Standards Applied Mathematics Series, vol. 12 (U. S. Government Printing Office, Washington, DC, 1951)
14. B.C. Wilson, G. Adam, A Monte Carlo model for the absorption and flux distributions of light in tissue. Med. Phys. **10**, 824–830 (1983)
15. J.M. Schmitt, A. Knüttel, M. Yadlowsky, M.A. Eckhaus, Optical-coherence tomography of a dense tissue: statistics of attenuation and backscattering. Phys. Med. Biol. **39**, 1705–1720 (1994)
16. H.T. Yura, Signal-to-noise ratio of heterodyne lidar systems in the presence of atmospheric turbulence. Opt. Acta **26**, 627–644 (1979)

17. Y. Feng, R. Wang, J. Elder, Theoretical model of optical coherence tomography for system optimization and characterization. J. Opt. Soc. Am. A **20**, 1792–1803 (2003)
18. B. Karamata, M. Laubscher, M. Leutenegger, S. Bourquin, T. Lasser, P. Lambelet, Multiple scattering in optical coherence tomography. I. Investigation and modeling. J. Opt. Soc. Am. A **22**, 1369–1379 (2005)
19. J.W. Goodman, *Statistical Optics* (Wiley, New York, 1985)
20. R.G. Frehlich, M.J. Kavaya, Coherent laser radar performance for general atmospheric refractive turbulence. Appl. Opt. **30**, 5325–5352 (1991)
21. D. Arnush, Underwater light-beam propagation in the small-angle-scattering approximation. J. Opt. Soc. Am. **62**, 1109–1111 (1972)
22. H.T. Yura, A multiple scattering analysis of the propagation of radiance through the atmosphere, in *Proceedings of the Union Radio-Scientifique Internationale Open Symposium*, La Baule, 1977, pp. 65–69
23. H.T. Yura, L. Thrane, P.E. Andersen, Closed-form solution for the Wigner phase-space distribution function for diffuse reflection and small-angle scattering in a random medium. J. Opt. Soc. Am. A **17**, 2464–2474 (2000)
24. M.G. Raymer, C. Cheng, D.M. Toloudis, M. Anderson, M. Beck, Propagation of Wigner coherence functions in multiple scattering media, in *Advances in Optical Imaging and Photon Migration*, vol. 2 of *OSA Trends in Optics and Photonics Series*, eds. by R.R. Alfano, J.G. Fujimoto (Optical Society of America, Washington, DC, 1996), pp. 236–238; C.-C. Cheng, M.G. Raymer, Long-range saturation of spatial decoherence in wave-field transport in random multiple-scattering media. Phys. Rev. Lett. **82**, 4807–4810 (1999); M.G. Raymer, C.-C. Cheng, Propagation of the optical Wigner function in random multiple-scattering media, in *Laser-Tissue Interaction XI: Photochemical*, *Photothermal, and Photomechanical*, eds. by D. D. Duncan, J.O. Hollinger, S.L. Jacques. Proc. SPIE **3914**, 376–380 (2000)
25. P.E. Andersen, T.M. Jørgensen, L. Thrane, A. Tycho, H.T. Yura, Modeling light–tissue interaction in optical coherence tomography systems, in *Optical Coherence Tomography: Technology and Applications*, ed. by W. Drexler, J.G. Fujimoto (Springer, New York, 2008), pp. 73–113 (Chap. 3). ISBN 3540775498
26. L. Thrane, H.T. Yura, P.E. Andersen, Optical coherence tomography: new analytical model and the shower curtain effect. Proc. SPIE **4001**, 202–208 (2000)
27. L. Thrane, H.T. Yura, P.E. Andersen, Calculation of the maximum obtainable probing depth of optical coherence tomography in tissue. Proc. SPIE **3915**, 2–11 (2000)
28. P.E. Andersen, L. Thrane, H.T. Yura, A. Tycho, T.M. Jørgensen, Modeling the optical coherence tomography geometry using the extended Huygens-Fresnel principle and Monte Carlo simulations. Proc. SPIE **3914**, 394–406 (2000)
29. H.T. Yura, Signal-to-noise ratio of heterodyne lidar systems in the presence of atmospheric turbulence. Opt. Acta **26**, 627–644 (1979)
30. I. Dror, A. Sandrov, N.S. Kopeika, Experimental investigation of the influence of the relative position of the scattering layer on image quality: the shower curtain effect. Appl. Opt. **37**, 6495–6499 (1998)
31. V.I. Tatarskii, *Wave Propagation in a Turbulent Medium* (McGraw-Hill, New York, 1961)
32. A. Ishimaru, *Wave Propagation and Scatteringin Random Media* (IEEE Press, Piscataway, 1997)
33. J. Strohbehn (ed.), *Laser Beam Propagation in the Atmosphere* (Springer, New York, 1978)
34. R.L. Fante, Wave propagation in random media: a systems approach, in *Progress in Optics XXII*, ed. by E. Wolf (Elsevier, New York, 1985)
35. J.M. Schmitt, G. Kumar, Turbulent nature of refractive-index variations in biological tissue. Opt. Lett. **21**, 1310–1312 (1996)
36. S.M. Rytov, Y.A. Kravtsov, V.I. Tatarskii, Principles of statistical radiophysics, in *Wave Propagation Through Random Media*, vol. 4 (Springer, Berlin, 1989)
37. R.F. Lutomirski, H.T. Yura, Propagation of a finite optical beam in an inhomogeneous medium. Appl. Opt. **10**, 1652–1658 (1971)

38. Z.I. Feizulin, Y.A. Kravtsov, Expansion of a laser beam in a turbulent medium. Izv. Vyssh. Uchebn. Zaved. Radiofiz. **24**, 1351–1355 (1967)
39. J.W. Goodman, *Introduction to Fourier Optics*, 2nd edn. (McGraw-Hill, Singapore, 1996)
40. H.T. Yura, S.G. Hanson, Optical beam wave propagation through complex optical systems. J. Opt. Soc. Am. A **4**, 1931–1948 (1987)
41. H.T. Yura, S.G. Hanson, Second-order statistics for wave propagation through complex optical systems. J. Opt. Soc. Am. A **6**, 564–575 (1989)
42. A.E. Siegman, *Lasers* (University Science, Mill Valley, 1986), pp. 626–630
43. M.J.C. Van Gemert, S.L. Jacques, H.J.C.M. Sterenborg, W.M. Star, Skin optics. IEEE Trans. Biomed. Eng. **36**, 1146–1154 (1989)
44. C.F. Bohren, D.R. Huffman, *Absorption and Scattering of Light by Small Particles* (Wiley, New York, 1983)
45. H.T. Yura, S.G. Hanson, Effects of receiver optics contamination on the performance of laser velocimeter systems. J. Opt. Soc. Am. A **13**, 1891–1902 (1996)
46. L. Thrane, Optical coherence tomography: modeling and applications, PhD dissertation Risø National Laboratory, Denmark, 2000. ISBN 87-550-2771-7
47. L.G. Henyey, J.L. Greenstein, Diffuse radiation in the galaxy. Astro-Phys. J. **93**, 70–83 (1941)
48. S.L. Jacques, C.A. Alter, S.A. Prahl, Angular dependence of He-Ne laser light scattering by human dermis. Lasers Life Sci. **1**, 309–333 (1987)
49. C.M. Sonnenschein, F.A. Horrigan, Signal-to-noise relationships for coaxial systems that heterodyne backscatter from the atmosphere. Appl. Opt. **10**, 1600–1604 (1971)
50. D.L. Fried, Optical heterodyne detection of an atmospherically distorted signal wave front. Proc. IEEE **55**, 57–67 (1967)
51. V.V. Tuchin, S.R. Utz, I.V. Yaroslavsky, Skin optics: modeling of light transport and measuring of optical parameters, in *Medical Optical Tomography: Functional Imaging and Monitoring*, ed. by G. Mueller, B. Chance, R. Alfano et al., vol. IS11 (SPIE Press, Bellingham, 1993), pp. 234–258
52. V.I. Tatarskii, *The Effects of the Turbulent Atmosphere on Wave Propagation* (National Technical Information Service, Springfield, 1971)
53. A. Tycho, T.M. Jørgensen, Comment on 'Excitation with a focused, pulsed optical beam in scattering media: diffraction effects. Appl. Opt. **41**, 4709–4711 (2002)
54. V.R. Daria, C. Saloma, S. Kawata, Excitation with a focused, pulsed optical beam in scattering media: diffraction effects. Appl. Opt. **39**, 5244–5255 (2000)
55. J. Schmitt, A. Knüttel, M. Yadlowski, Confocal microscopy in turbid media. J. Opt. Soc. A **11**, 2226–2235 (1994)
56. J.M. Schmitt, K. Ben-Letaief, Efficient Monte Carlo simulation of confocal microscopy in biological tissue. J. Opt. Soc. Am. A **13**, 952–961 (1996)
57. C.M. Blanca, C. Saloma, Monte Carlo analysis of two-photon fluorescence imaging through a scattering medium. Appl. Opt. **37**, 8092–8102 (1998)
58. Y. Pan, R. Birngruber, J. Rosperich, R. Engelhardt, Low-coherence optical tomography in turbid tissue – theoretical analysis. Appl. Opt. **34**, 6564–6574 (1995)
59. G. Yao, L.V. Wang, Monte Carlo simulation of an optical coherence tomography signal in homogeneous turbid media. Phys. Med. Biol. **44**, 2307–2320 (1999)
60. Z. Song, K. Dong, X.H. Hu, J.Q. Lu, Monte Carlo simulation of converging laser beams propagating in biological materials. Appl. Opt. **38**, 2944–2949 (1999)
61. C.M. Blanca, C. Saloma, Efficient analysis of temporal broadening of a pulsed focused Gaussian beam in scattering media. Appl. Opt. **38**, 5433–5437 (1999)
62. L.V. Wang, G. Liang, Absorption distribution of an optical beam focused into a turbid medium. Appl. Opt. **38**, 4951–4958 (1999)
63. A.K. Dunn, C. Smithpeter, A.J. Welch, R. Richards-Kortum, Sources of contrast in confocal reflectance imaging. Appl. Opt. **35**, 3441–3446 (1996)
64. L.-H. Wang, S.L. Jacques, L.-Q. Zheng, MCML – Monte Carlo modeling of photon transport in multi-layered tissues. Comput. Methods Programs Biomed. **47**, 131–146 (1995)

65. S.A. Prahl, M. Keijzer, S.L. Jacques, A.J. Welch, A Monte Carlo model for light propagation in tissue, in *Dosimetry of Laser Radiation in Medicine and Biology*, ed. by S.A. Prahl. SPIE Institute Series, vol. IS5 (SPIE Press, Bellingham, 1998)
66. D.I. Hughes, F.A. Duck, Automatic attenuation compensation for ultrasonic imaging. Ultrasound Med. Biol. **23**, 651–664 (1997)
67. L. Thrane, T.M. Jørgensen, P.E. Andersen, H.T. Yura, True-reflection OCT imaging. Proc. SPIE **4619**, 36–42 (2002)
68. S.A. Prahl, M.J.C. van Gemert, A.J. Welch, Determining the optical properties of turbid media by using the adding-doubling method. Appl. Opt. **32**, 559–568 (1993)
69. J.M. Schmitt, S.H. Xiang, K.M. Yung, Speckle in optical coherence tomography. J. Biomed. Opt. **4**, 95–105 (1999)
70. L. Thrane, M.H. Frosz, A. Tycho, T.M. Jørgensen, H.T. Yura, P.E. Andersen, Extraction of optical scattering parameters and attenuation compensation in optical coherence tomography images of multi-layered tissue structures. Opt. Lett. **29**, 1641–1643 (2004)
71. G.J. Tearney, S.A. Boppart, B.E. Bouma, M.E. Brezinski, N.J. Weissman, J.F. Southern, J.G. Fujimoto, Scanning single-mode fiber optic catheter-endoscope for optical coherence tomography. Opt. Lett. **21**, 543–545 (1996)
72. R.O. Esenaliev, K.V. Larin, I.V. Larina, M. Motamedi, Noninvasive monitoring of glucose concentration with optical coherence tomography. Opt. Lett. **26**, 992–994 (2001)
73. K.V. Larin, T. Akkin, R.O. Esenaliev, M. Motamedi, T.E. Milner, Phase-sensitive optical low-coherence reflectometry for the detection of analyte concentrations. Appl. Opt. **43**, 3408–3414 (2004)
74. D.J. Faber, M.C.G. Aalders, E.G. Mik, B.A. Hooper, M.J.C. van Gemert, T.G. van Leeuwen, Oxygen saturation-dependent absorption and scattering of blood. Phys. Rev. Lett. **93**, 028102-1–028102-4 (2004)
75. D.J. Faber, E.G. Mik, M.C.G. Aalders, T.G. van Leeuwen, Toward assessment of blood oxygen saturation by spectroscopic optical coherence tomography. Opt. Lett. **30**, 1015–1017 (2005)
76. D.J. Faber, T.G. van Leeuwen, Are quantitative attenuation measurements of blood by optical coherence tomography feasible? Opt. Lett. **34**, 1435–1437 (2009)
77. V.M. Kodach, D.J. Faber, J. van Marle, T.G. van Leeuwen, J. Kalkman, Determination of the scattering anisotropy with optical coherence tomography. Opt. Express **19**, 6131–6140 (2011)
78. F.J. van der Meer, D.J. Faber, D.M.B. Sassoon, M.C. Aalders, G. Pasterkamp, T.G. van Leeuwen, Localized measurement of optical attenuation coefficients of atherosclerotic plaque constituents by quantitative optical coherence tomography. IEEE Trans. Med. Imaging **24**, 1369–1376 (2005)
79. N.M. Shakhova, V.M. Gelikonov, V.A. Kamensky, R.V. Kuranov, I.V. Turchin, Clinical aspects of the endoscopic optical coherence tomography: a method for improving the diagnostic efficiency. Laser Phys. **12**, 617–626 (2002)
80. D. Levitz, L. Thrane, M.H. Frosz, P.E. Andersen, C.B. Andersen, J. Valanciunaite, J. Swartling, S. Andersson-Engels, P.R. Hansen, Determination of optical scattering properties of highly-scattering media in optical coherence tomography images. Opt. Express **12**, 249–259 (2004)
81. R. Samatham, S.L. Jacques, P. Campagnola, Optical properties of mutant versus wild-type mouse skin measured by reflectance-mode confocal scanning laser microscopy (rCSLM). J. Biomed. Opt. **13**, 041309 (2008)
82. A. Knüttel, S. Bonev, W. Knaak, New method for evaluation of in vivo scattering and refractive index properties obtained with optical coherence tomography. J. Biomed. Opt. **9**, 265–273 (2004)
83. E.P. Wigner, On the quantum correction for thermodynamic equilibrium. Phys. Rev. **40**, 749–759 (1932)
84. S. John, G. Pang, Y. Yang, Optical coherence propagation and imaging in a multiple scattering medium. J. Biomed. Opt. **1**, 180–191 (1996)

85. A. Wax, J.E. Thomas, Measurement of smoothed Wigner phase-space distributions for small-angle scattering in a turbid medium. J. Opt. Soc. Am. A **15**, 1896–1908 (1998)
86. C.-C. Cheng, M.G. Raymer, Propagation of transverse optical coherence in random multiple-scattering media. Phys. Rev. A **62**, 023811-1–023811-12 (2000)
87. M. Hillery, R.F. O'Connel, M.O. Scully, E.P. Wigner, Distribution functions in physics: fundamentals. Phys. Rep. **106**, 121–167 (1984)
88. V.A. Banakh, V.L. Mironov, *LIDAR in a Turbulent Atmosphere* (Artech House, Boston, 1987)